Searches for Exotic Mesons at CLAS12

Charlie Velasquez

MSc by Research

University of York
Physics, Engineering and Technology

September 2024

Abstract

The Standard Model proposes the quarks, leptons and bosons to account for all matter and nearly all the fundamental forces. With the existence and expected behaviour of these particles experimentally confirmed, the Standard Model is highly successful and is the leading theory of elementary particle physics. The hadrons are a family of composite particles comprised of the mesons and the baryons which can be modelled as bound states of quarks. The constituent quark model describes mesons as quark-antiquark pairs and baryons as three quarks; it's a simple but successful model, accounting for almost all of the experimentally confirmed hadrons. Quantum chromodynamics (QCD), the theory of the strong force belonging to the Standard Model, develops on the constituent quark model by introducing the strong force mediator particle known as the gluon. As a result, QCD predicts additional hadrons which are termed exotics. The subject of the research presented in this thesis is to search for exotic mesons produced in electron-proton scattering at CLAS12 at Jefferson Lab.

The $ep \rightarrow epK^+K^-$ reaction was chosen as the reaction of interest. By using the CLAS12 Forward Tagger, reactions were chosen with electrons scattering at low angles so that a quasi-real photon mediated the electron-proton interaction. During this interaction, various types of mesons are produced which all contribute to the final state of the reaction of interest. Several analysis techniques were applied to the experimental data to ensure that only the reaction of interest was studied. Moments of angular distribution were obtained and are presented in this thesis. These distributions show the contributions of different types of mesons to the final state, meaning that signatures of non-exotic and exotic mesons can be observed.

Table of contents

List of figures

List of tables

Dedication

I would like to dedicate this thesis to my parents and my grandparents who have always supported and inspired me.

Declaration

I declare that this thesis is a presentation of original work and I am the sole author. This work has not previously been presented for an award at this, or any other, University. All sources are acknowledged as References.

Chapter 1

Introduction

The search for exotic mesons is the subject of the research presented in this thesis. This subject is part of the broader subject known as hadron spectroscopy which concerns the discovery, classification and study of the hadrons; it is a primary focus of the research conducted at Jefferson Lab. In this chapter, important concepts such as the Standard Model, quantum chromodynamics and exotic mesons are introduced.

1.1 Hadrons

At present, the leading theory in particle physics is the Standard Model. This theory proposes 17 fundamental particles that constitute all matter and nearly all forces; the 6 quarks, the 6 leptons, the 4 gauge bosons and the Higgs boson. All of the quarks and leptons have spin 1/2, hence they obey Fermi statistics and can be grouped into a family of particles known as the fermions. Every fermion has an antiparticle which is identical but has an opposite electric charge. The gauge bosons all have spin 1 and the Higgs boson, the only known scalar boson, has spin 0 [1]. All of these fundamental particles have been experimentally detected, the latest being the Higgs boson which was observed at the LHC in 2012 [2].

The six types of quarks, also known as the flavours, are up, down, strange, charm, bottom and top. Similarly, the leptons have six flavours: the electron, muon, tau (the three charged leptons) and three different types of neutrinos. Information on quark and lepton flavours can be found in Tabl. 1.1. All the flavours of the quarks and the charged leptons interact via the electromagnetic and the weak forces; additionally, quarks interact via the strong force due to a property they possess known as

Table 1.1 Properties of the quarks and leptons in the Standard Model. Charge is given in units of the elementary charge e, the negative electric charge carried by a single electron. Neutrinos are omitted; they have zero charge and in the Standard Model they are massless [3].

Quarks	Charge (e)	Mass (MeV/c)
up	2/3	2.16
down	-1/3	4.67
strange	-1/3	93
charm	2/3	1270
bottom	-1/3	4180
top	2/3	172760
Leptons		
electron	-1	0.511
muon	-1	105.7
tau	-1	1776.9

colour charge. Colour charge permits particles to interact via the strong force, analogous to the electric charge for the electromagnetic force. The Standard Model postulates that three of the four fundamental forces, the weak, strong and electromagnetic forces, are mediated by four fundamental particles, the aforementioned gauge bosons. The W and Z bosons mediate the weak force, the photon (γ) mediates the electromagnetic force and the gluon (g) mediates the strong force. Information on these mediator particles can be found in Tabl. 1.2. Mediator particles are exchanged when fermions interact; allowed interactions can be represented using Feynman diagrams.

Table 1.2 Properties of the gauge bosons in the Standard Model. Charge is given in units of the elementary charge e, the negative electric charge carried by a single electron [3].

Gauge Bosons	Charge (e)	Mass (GeV/c)
$W^{\pm}$	± 1	80.4
Z	0	91.2
photon	0	0
gluon	0	0

Presently, it's understood that through the strong interaction, quarks form bound states known as mesons and baryons or collectively as hadrons. A model known as the constituent quark model can be used to describe the structure of the hadrons. The constituent quark model states that mesons and baryons are the combinations of quarks, q, and antiquarks, $\bar{q}$, that are allowed under certain conditions. In this model, a meson is a quark-antiquark pair, $q\bar{q}$, and a baryon is a group of three quarks, qqq. Discoveries of mesons and baryons have long predated the postulation of the quark

model. Once the proton was discovered by Ernest Rutherford in 1919, the following 50 years of experimental efforts saw the discovery of numerous particles, culminating with the observation of quarks at SLAC in 1969. Notable discoveries throughout this period include that of the pion, the kaon and the lambda [4]. Information on experimentally detected mesons can be found in Tabl. 1.3. Alongside these experimental efforts, theoretical endeavours proved equally significant. In 1961, Murray Gell-Man introduced the eightfold to way simplify the description of this growing collection of baryons and mesons [5]. Groups of some of the lightest mesons and baryons can be shown using diagrammatic representations of the eightfold way, these are known as octets and are shown in Fig. 1.1. Developing on this work, three years later he put forward the concept of quarks; fundamental particles that congregate to form the proton and neutron, each possessing a fraction of the electric charge and mass [6].

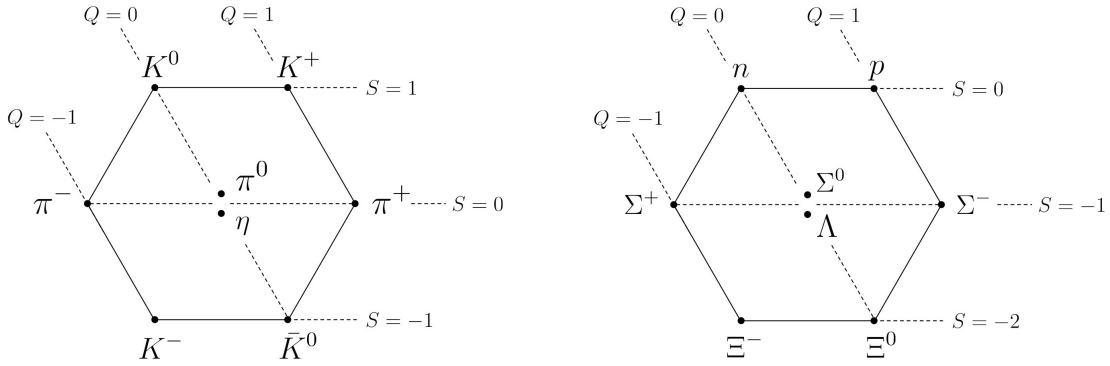

Fig. 1.1 Octets for the pseudoscalar, $J=0$, mesons (left) and lightest $J=1/2$ baryons (right) represented using the eightfold way. Q is the charge which is constant along each dashed diagonal line, S is the strangeness which is constant along each dashed horizontal line, B is the baryon number, and I_3 is the third component of the isospin.

1.1.1 The Constituent Quark Model

As previously mentioned, the constituent quark model states that a meson is a quark-antiquark pair, $q\bar{q}$, and a baryon is a group of three quarks, qqq. These two types of quark combinations belong to a group of allowed combinations which results after imposing a strict condition known as colour confinement. Quarks can exist in 'red', r, 'green', g, or 'blue', b, colour states and antiquarks in the $\bar{r}$,$\bar{g}$ or $\bar{b}$ colour states. The hypothesis of colour confinement is that hadrons can only exist in states known as colour singlets which have an overall colour charge of zero. This is seen in the

Table 1.3 Experimental mass spectrum of some of the lightest hadrons [3].

Meson	Spin	Parity	Strangeness	Charge (e)	Mass (MeV)
π^0	0	-1	0	0	134.98
$\pi^\pm$	0	-1	0	±1	139.57
$K^\pm$	0	-1	±1	±1	493.67
K^0	0	-1	+1	0	497.61
$\bar{K}^0$	0	-1	-1	0	497.61
η	0	-1	0	0	547.86
$\rho^\pm$	1	-1	0	±1	775.11
ρ^0	1	-1	0	0	775.26
Baryon					
p	1/2	-1	0	1	938.27
n	1/2	-1	0	0	939.57
Λ	1/2	-1	-1	0	1115.683

aforementioned quark combinations; if each quark in qqq is in a different colour state then the total colour charge is zero and if the quarks in $q\bar{q}$ have opposite colour charge then the total colour charge is zero. It follows that states such as qq, $q\bar{q}\bar{q}$, $qq\bar{q}$ and $qqqq$ are forbidden in the constituent quark model. Also note that these states possess fractional electric charge which, despite extensive searches, has never been observed for any composite particle. Interestingly, combinations such as $qq\bar{q}\bar{q}$ and $qqqq\bar{q}$ are allowed and are known as exotic states, these will be elaborated on in the next section, Sec. 1.2. The hypothesis of colour confinement also implies that quarks must exist within these states since an isolated quark has a non-zero colour charge [3],[1]. The existence of colour states has been observed directly by comparing the experimental and theoretical values of the differential cross-section of $e^+e^- \rightarrow \mu^+\mu^-$. The study completed by H.-J. Berend et al. in [7] showed that the Standard Model correctly predicts the cross-section and hence corroborates the existence of colour states. Now that quark combinations have been detailed and assigned to the mesons and baryons, the constituent quark model will be used to obtain the properties of some of the lightest mesons. To do this, we restrict ourselves to the lightest quarks, the up, down and strange quarks. Associated with a meson are several important quantum numbers, the total angular momentum J, the orbital angular momentum L and the vector sum of the quark spins S. The total angular momentum J of the meson is identified as the spin of the meson given in Tabl. 1.3 and is given by,

$$\mathbf{J} = \mathbf{L} + \mathbf{S} = |L-S|,\ \ |L-S+1|,\ \ |L-S+2|,\ \ \ldots,\ \ |L+S|. \tag{1.1}$$

In the centre-of-mass frame of the quark-antiquark pair, there is a single orbital angular momentum L. In this pair, each constituent quark has spin 1/2. These spins may be anti-aligned, resulting in $S = 0$, or aligned, resulting in $S = 1$. To describe the properties of the lightest mesons, the lowest-lying states of a quark-antiquark system, i.e. those with $L = 0$, are considered. By Eq. (1.1), $L = 0$ and $S = 0$ gives $J = 0$ which is the spin corresponding to the pseudoscalar mesons shown in Fig. 1.1. Therefore, the pseudoscalar mesons can be described by a quark-antiquark system with $L = 0$ and $S = 0$. Two additional properties of the mesons can be obtained using this model, these are the the parity P and the charge conjugation parity, also known as C-parity, C. The parity is given by

$$P = (-1)^{L+1}, \tag{1.2}$$

and the C-parity is given by,

$$C = (-1)^{L}, \tag{1.3}$$

where L is the orbital angular momentum in both equations. The parity of the negatively-charge pion π^- has been determined experimentally by W. Chinowsky and J. Steinberger who first observed the reaction

$$\pi^- + d \rightarrow 2n \tag{1.4}$$

as detailed in [8]. By imposing the conservation of parity and the conservation of angular momentum on the reaction given by Eq. (1.4), it can be ascertained that $P_{\pi^-} = -1$. Similar methods may be used to obtain the parities of other mesons and baryons, these are given in Tabl. 1.3. As mentioned previously, the pseudoscalar mesons can be described by a quark-antiquark system with $L = 0$ and $S = 0$. The parity and C-parity of this system can be calculated using Eq. (1.2) and Eq. (1.3) to get $P_{J=0} = -1$ and $C_{J=0} = 1$, which agree with the experimental parities. Within the pseudoscalar octet, a meson can be individually distinguished by determining its quark composition. To accomplish this, the charge Q and two new quantum numbers are required: the strangeness S and the third component of the isospin I_3. The up quark has $I_3 = 1/2$ and the down quark has $I_3 = -1/2$; both have $S = 0$. The strange quark has $I_3 = 1/2$ and $S = -1$. Values for Q of the quarks can be found in Tabl. 1.1. Subsequently, quark combinations can be deduced that have quantum numbers equal to those for the mesons given in Fig. 1.1. For example, the following quark combinations

$$\pi^- = \bar{u}d \qquad \pi^+ = u\bar{d} \qquad K^0 = d\bar{s} \qquad K^+ = u\bar{s} \tag{1.5}$$

return the correct values for Q, S and I_3. This process may be continued for the lightest 18 mesons and lightest 18 baryons to obtain quantum numbers that match exactly to experimental results. Whilst a resounding success in its description of many properties of the hadrons, the constituent quark model doesn't propose a mechanism that describes how quarks form bound states. Additionally, the masses of the quark combinations given in Eq. (1.5) are substantially lower than the experimentally confirmed masses of the hadrons they describe. Fortunately, a model known as quantum chromodynamics provides a much more suitable description of the hadrons.

1.1.2 Quantum Chromodynamics

Quantum chromodynamics (QCD) is a gauge theory that describes the strong force of the Standard Model. QCD can be formulated in Lagrangian field theory which means it has an associated Lagrangian. The equations that describe the dynamics of strongly interacting particles can be extracted from the QCD Lagrangian. However, mathematical derivations such as these are outside of the scope of this thesis so will be avoided and instead, a more phenomenological approach will be taken to describe the theory of the strong force.

QCD introduces the gluon, the mediator of the strong force. There are eight gluons, each a different mixture of the three colour states, which interact with particles that have colour, such as the quarks. As the gluons themselves possess colour, this implies that gluons can interact with themselves or with other gluons, a property known as self-interaction. This property allows for certain types of quark-quark scattering interactions where the net effect of these interactions results in an antiscreening effect. This effect varies by distance from the source and thus strong force interactions are weaker at short distances than they are at long distances. This is an important property of the strong force known as asymptotic freedom, first identified by Gross and Wilczek, and Politzer [9],[10].

The previously mentioned property of colour confinement is also an important property of QCD. The union of confinement and gluon self-interactions implies that two or more gluons can combine to form colourless states, composed purely of gluons, known as glueballs. The hadrons can be described by QCD when colour confinement is imposed, similarly as in the constituent quark model. Furthermore, gluons can contribute to the quantum numbers of quark-antiquark pairs, forming states known as hybrid states [11]. Glueballs and hybrids will be elaborated on in Sec. 1.2.

The final feature of QCD that will be mentioned is the mass generation of the hadrons. A model known as the bag model can be used to obtain an accurate mass spectrum of some of the lightest

hadrons. In this model, quarks are confined to a 'bubble' or 'bag' which is under pressure from a surrounding vacuum region which arises due to confinement. This pressure is balanced by the counterpressure of the kinetic energy of the quarks inside the bag. The model has the following conditions: the u and d quarks are massless, the s quark has a finite mass, the quarks are considered as free particles moving at relativistic speeds, the interactions between the quark are considered, and the zero-point energy of quantum fields inside the bag are considered [12]. A diagram of the bag model for a baryon is shown in Fig. 1.2a. A successful bag model developed at MIT, known as the MIT bag model, was introduced by Chodos et al., in 1974 [13]. In 1983, the MIT bag model was used to produce the correct masses of some of the lightest hadrons which are shown in Fig. 1.2b. Modern computational methods can be used to obtain a wider and more accurate spectrum of hadron masses predicted by QCD as will be discussed in section 1.2.

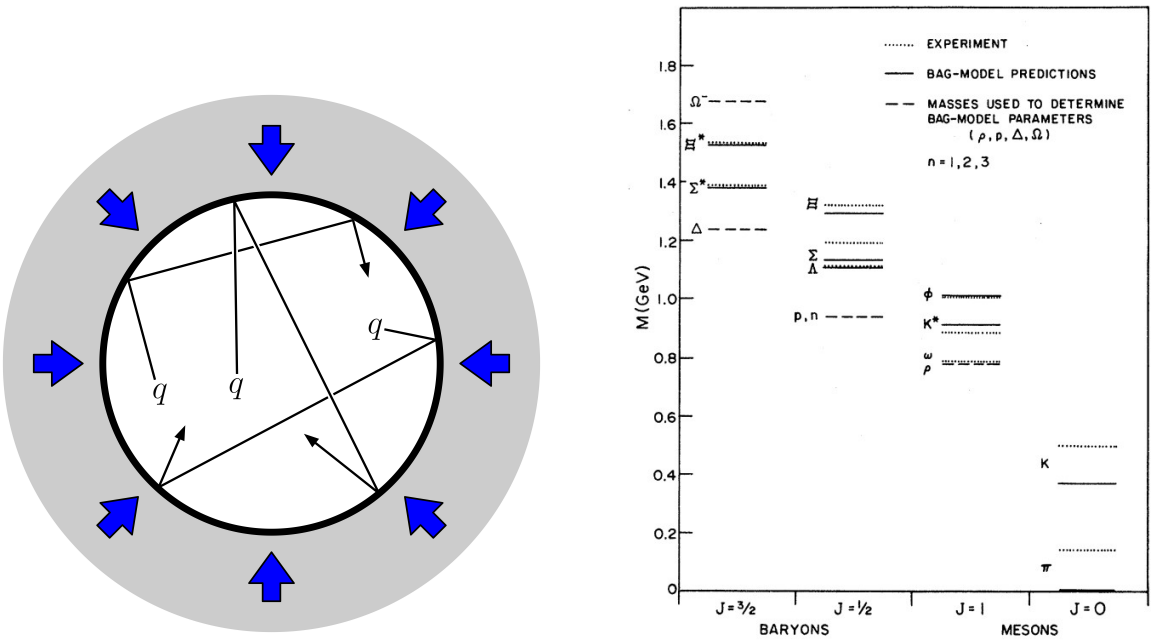

(a) A diagram of the bag model

(b) The hadron spectrum from the MIT bag model

Fig. 1.2 A diagram of the bag model (a) showing the quarks travelling within the bag and the pressure (blue arrows) caused by the presence of a region of surrounding vacuum (grey) resulting from the confinement principle. The hadron spectrum calculated using the MIT bag model (b) [14].

1.2 Exotic Composite Particles

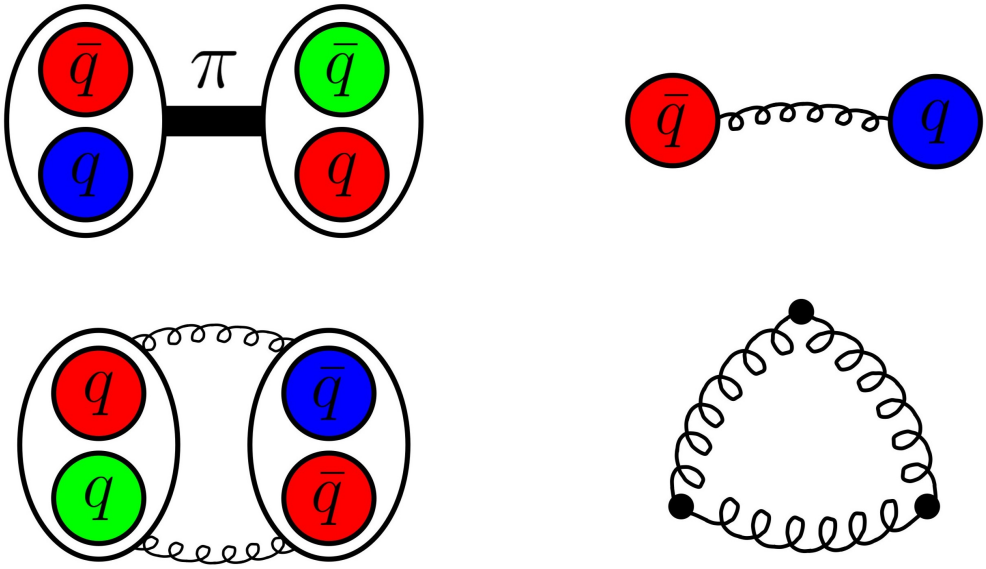

Fig. 1.3 Four diagrams of exotic mesons: tetraquarks – two quark-antiquark pairs bound by long-range meson exchanges (top left) and diquark and anti-diquark bound by gluons (bottom left), a hybrid (top right) and a glueball (bottom right).

QCD allows for exotic states that are far more complicated and numerous than the states predicted by the constituent quark model. The properties of these many states can be determined through advanced computational methods.

In the constituent quark model, a meson is a quark-antiquark pair $q\bar{q}$. This system has the quantum numbers J, P and C which can be conveniently written as J^{PC}. For example, by considering the discussion in the previous section, π^- has $J^{PC} = 0^{-+}$ which is an example of an allowed J^{PC} state. The equations for J, P and C given in Sec. 1.1 permit a collection of allowed J^{PC} quantum numbers, some of which are

$$J^{PC} = 0^{-+},\ 0^{++},\ 1^{--},\ 1^{+-},\ 1^{++},\ 2^{--},\ 2^{-+},\ 2^{++},\ldots\ . \tag{1.6}$$

Similarly, a collection of J^{PC} quantum numbers that are forbidden by the equations for J, P and C can be obtained, some of which are,

$$J^{PC} = 0^{--},\ 0^{+-},\ 1^{-+},\ 2^{+-},\ldots\ . \tag{1.7}$$

An exotic meson is a meson that cannot be described solely by the simple quark-antiquark system propounded by the constituent quark model. Additionally, an exotic meson may have an allowed J^{PC} or a forbidden J^{PC}. QCD predicts novel states such as tetraquarks, hybrids and glueballs which are all classified as exotic mesons.

A tetraquark is a diquark and anti-diquark bound by gluon exchanges, $qq\bar{q}\bar{q}$, or two quark-antiquark pairs bound by long-range meson exchanges, $q\bar{q}q\bar{q}$, known as a molecular state. Hybrids are quark-antiquark pairs joined to excited gluons and glueballs are two or more gluons bound together. At present, two leading tetraquark candidates are $a_0(980)$ and $f_0(980)$ however it is unknown whether these mesons have a $qq\bar{q}\bar{q}$ configuration or are instead the molecular state $K\bar{K}$. Diagrams of these exotic mesons are shown in Fig. 1.3

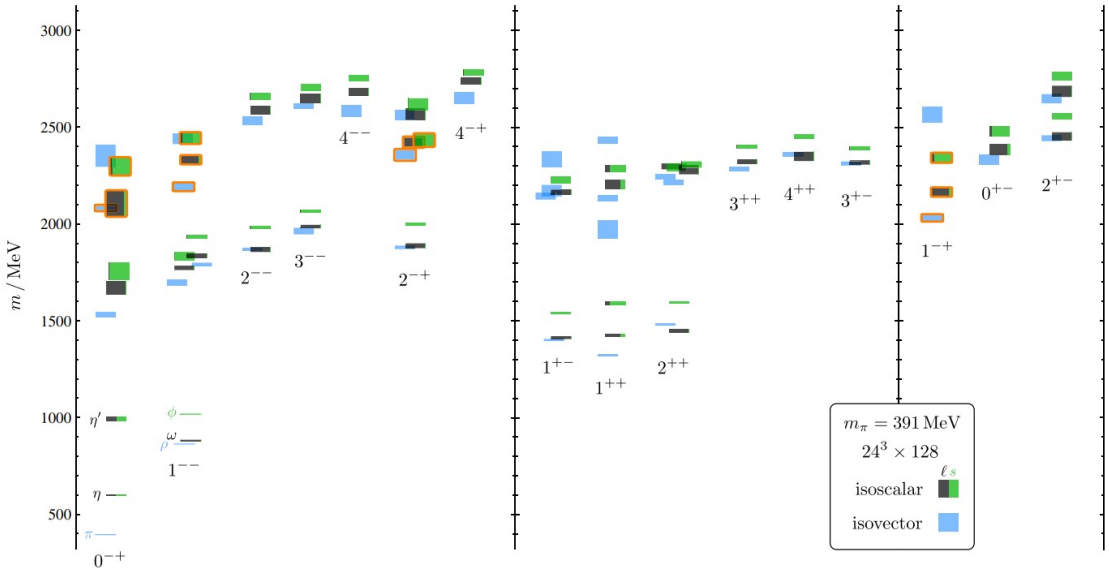

Fig. 1.4 Theoretical meson spectrum, including those non-exotics (left and middle region) and exotics (right region), obtained through LQCD calculations. The orange boxes indicate mesons that may overlap with $q\bar{q}$ states coupled to a gluon [15].

Before discussing hybrids and glueballs, lattice QCD (LQCD) will be introduced. In brief, LQCD uses a discrete space-time with quarks situated at points and gluons represented by links joining the

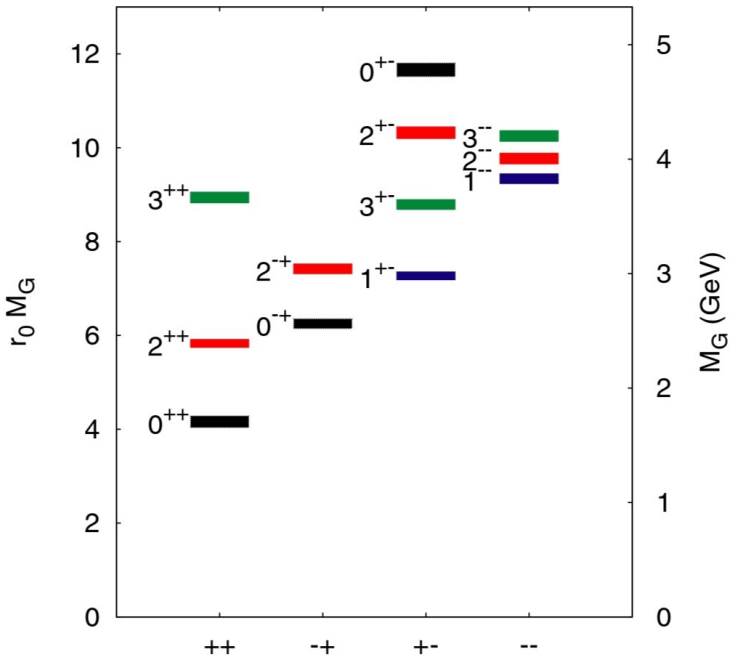

Fig. 1.5 Theoretical glueball mass spectrum, including those with non-exotic and exotic J^{PC}, obtained through LQCD calculations [16].

points. This structure allows for a discretised version of the QCD Lagrangian to be used to describe the dynamics of the quarks and gluons. Subsequently, by making use of advanced computational methods, the mass and quantum numbers of hadrons predicted by QCD can be determined.

LQCD calculations predict a 1^{-+} hybrid with a mass of 1.9 ± 0.1 GeV [17]. The two leading candidates for this hybrid are $\pi_1(1400)$ and $\pi_1(1600)$, each with a broad mass range as expected for hybrids. The masses of various non-exotic and exotic mesons were calculated by Jozef J. Dudek et al in [15]. The authors extracted a meson spectrum, Fig. 1.4, using LQCD. LQCD can also be used to calculate the mass of glueballs predicted by QCD which are shown in Fig. 1.5. The lightest glueballs, the non-exotic scalar $J^{PC} = 0^{++}$ and tensor 2^{++}, are predicted to have masses around 1600 and 2300 MeV respectively. The first exotic glueball 0^{+-} is predicted to have a mass of about 4800 MeV. Additionally, LQCD calculations show that glueballs couple to isospin singlet mesons (I=0), known as isoscalar mesons, with the same quantum numbers and which are similar in mass. For example, the 0^{++} glueball and the two $0++$ isoscalar mesons, which are all near 1500 MeV, couple together and mix to produce the observed states $f_0(1370)$, $f_0(1500)$, and $f_0(1710)$ [3].

1.3 Exotic Meson Photoproduction

There have been various exotic meson searches put forward over the past few decades. It has been suggested that hybrids may be produced in nucleon-antinucleon annihilation as this reaction is a copious source of gluons and that scalar glueballs may be present in the states produced in the decay of J/ψ [18],[19]. There are many experiments that have searched for exotic mesons as detailed in Sec. 1.4.

The research presented in this thesis concerns the quasi-real photoproduction of exotic mesons on a proton. The term quasi-real refers to a photon with a virtuality $Q^2 < 1(GeV/c)^2$, this kinematic region is known as the quasi-real photoproduction region. A low Q^2 photon may be emitted by an electron scattering at a low angle off a proton [20]. Due to the low Q^2, the scattered electron retains its polarisation information which can be measured after it scatters. The reaction (channel) studied in this research was $ep \to epK^+K^-$; a possible Feynman diagram for this reaction is shown in Fig. 1.6. Feynman diagrams are pictorial representations of the possible interactions that may occur between the initial state particles (the leftmost particles in the diagram) to produce the final state particles (the rightmost particles in the diagram). Particles that occur in the diagram but are not in the initial or final state are known as resonances. In Fig. 1.6, the electron e and proton p are initial state particles,

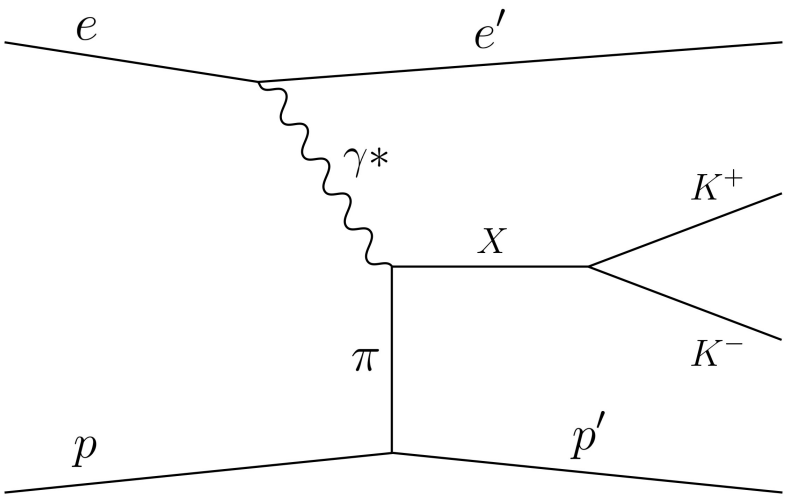

Fig. 1.6 Feynman diagram of a possible interaction associated with the reaction of interest. The quasi-real photon is represented by γ^* and the meson by X.

the arbitrary meson represented by X is a resonance, and the scattered electron e', scattered proton p', K^+ and K^- are final state particles. For a set of initial particles, there are usually many suitable Feynman diagrams corresponding to the many allowed interactions that may take place. These may be represented by replacing the arbitrary meson X, which is used as a placeholder, with the meson involved in the chosen interaction. For example, the meson X may be replaced with the meson $\phi(1020)$ which has $\phi \to K^+K^-$ as its most common decay [3]. Alternatively, this meson X may be an exotic, as shown by Szczepaniak and Swat in [21]. In this paper, the authors demonstrate that a greater proportion of exotic mesons are produced in photoproduction experiments than in hadroproduction experiments due to the photon being a spin 1 particle.

In scattering experiments, the reaction of interest will occur alongside many other possible reactions, such as $ep \to N\pi\pi$, where N can be either a proton or neutron. Therefore, a large assortment of mesons will be produced and detected. To disentangle this complicated assortment, the identity of the specific mesons involved can be uncovered by determining two quantities, the moments of angular distributions and the partial waves. The moments of angular distributions, henceforth referred to as moments, can be obtained using the information on the polarisation of the quasi-real photon and the angular distribution of the koans. The moments provide the contributions of the partial waves that make up the assortment of mesons. The partial waves are directly linked to a mesons quantum number and the ones studied in research presented in this thesis are the S, P and D waves. A more detailed description of moments will be provided in Sec 4.3.

1.4 History of Exotic Meson Searches

The possibility of the existence of exotic mesons was first suggested by Gell-Man alongside the introduction of the quark model. Since then there have been numerous theoretical and phenomenological investigations into exotic mesons, and experimental searches for indications of the existence of exotic mesons. Developing on the concepts of Gell-Mann, R. J. Jaffe used the bag model to suggest a light exotic nonet similar to the nonet in Fig. 1.1 but comprised entirely of tetraquarks [22]. The experimental efforts are just as impressive, and some examples are provided in this section.

Since the 1980s, a few exotic mesons have been observed across various experimental searches. Evidence of the $\pi_1(1400)$ $J^{PC} = 1^{-+}$ hybrid candidate mentioned in Sec. 1.2 was first observed in 1988 by the GAMS programme at CERN. In the experiment, a 100 GeV momentum π^- beam

was struck against a liquid hydrogen target to induce the reaction $N\pi^- \to \eta\pi^- N$, partial wave analysis of the final state indicated the existence of a 1^{-+} state with mass 1406±20 MeV and width 180±30 MeV. Subsequently, similar experiments were conducted by The High Energy Accelerator Research Organisation (KEK) in 1992, the VES Collaboration at the Institute for High Energy Physics (IHEP) in 1996, and the E852 Collaboration at Brookhaven National Laboratory (BNL) in 1997. Each experiment produced similar evidence suggesting the existence of the exotic 1^{-+} meson with a mass near 1400 MeV. It was the Crystal Barrel Experiment at CERN that confirmed the existence of $\pi_1(1400)$ in 1997 by stopping antiprotons in liquid deuterium to induce the reaction $\bar{p}n \to \pi^-\pi^0\eta$. Partial wave analysis of the final state of this reaction indicated that the $\pi\eta$ possessed resonant behaviour with the exotic quantum numbers 1^{-+}, corresponding to $\pi_1(1400)$ [23],[24],[25].

The other 1^{-+} hybrid mentioned in Sec. 1.2, $\pi_1(1600)$, was detected alongside $\pi_1(1400)$ in the 1996 VES Collaboration experiment. A higher energy pion beam was used and the final state of $N\pi^- \to \eta'\pi^- N$ was investigated resulting in the identification of a state with 1^{-+} and a mass near 1600 MeV. Similar methods and results were reported by the E852 Collaboration and Crystal Barrel Experiment. More recently, the COMPASS collaboration at CERN also detected $\pi_1(1600)$ in 2004 and later in 2010. In this experiment, a 190 GeV pion beam impinged against a lead target to induce $\pi^- Pb \to \pi^-\pi^-\pi^+$, partial wave analysis conducted on the final state revealed a 1^{-+} meson with mass 1660±10 MeV corresponding to $\pi_1(1600)$ [26].

Glueballs are also the subject of various experimental searches and in 2024 the Beijing-based BESIII collaboration reported the first possible detection of the lightest glueball, $X(2370)$ with $J^{PC} = 0^{-+}$. The collaboration conducted partial wave analysis on the J/ψ decay channel $J\psi \to \gamma K_s^0 K_s^0 \eta'$ to observe $X(2370)$ with mass 2395±11 MeV which is similar to the mass of the 0^{-+} glueball predicted by LQCD seen in Fig. 1.5 [27].

Chapter 2

Experimental Setup at Jefferson Laboratory

The research presented in this thesis involved the analysis of data taken by the CLAS collaboration for the MesonEx project using the CLAS12 spectrometer located in Hall B at Jefferson Laboratory. In this chapter, the experimental setup and software framework at Jefferson Laboratory will be detailed.

2.1 Jefferson Laboratory

Fig. 2.1 An aerial photo of Jefferson Laboratory [28].

The Thomas Jefferson National Accelerator Facility, Fig. 2.1, also known as Jefferson Laboratory or JLab, is located in Newport News, Virginia and conducts experimental investigations into fundamental concepts of nuclear and particle physics. Since the 1990s, Jefferson Lab has delivered the world's most intense and precise electron beam in the multi-GeV region. The beam is produced by the CEBAF accelerator and is split among four Halls: Hall A, Hall B, Hall C and Hall D, which are each responsible for investigating various concepts such as nuclear structure, hadron spectroscopy and hyperon spectroscopy. The impressive catalogue of research conducted by physicists at Jefferson Laboratory includes contributions to the proton charge radius puzzle, the study of pentaquarks in the $J/\psi - 007$ experiment and the measurement of valance quark PDFs in the MARATHON experiment [29],[30].

2.2 CEBAF

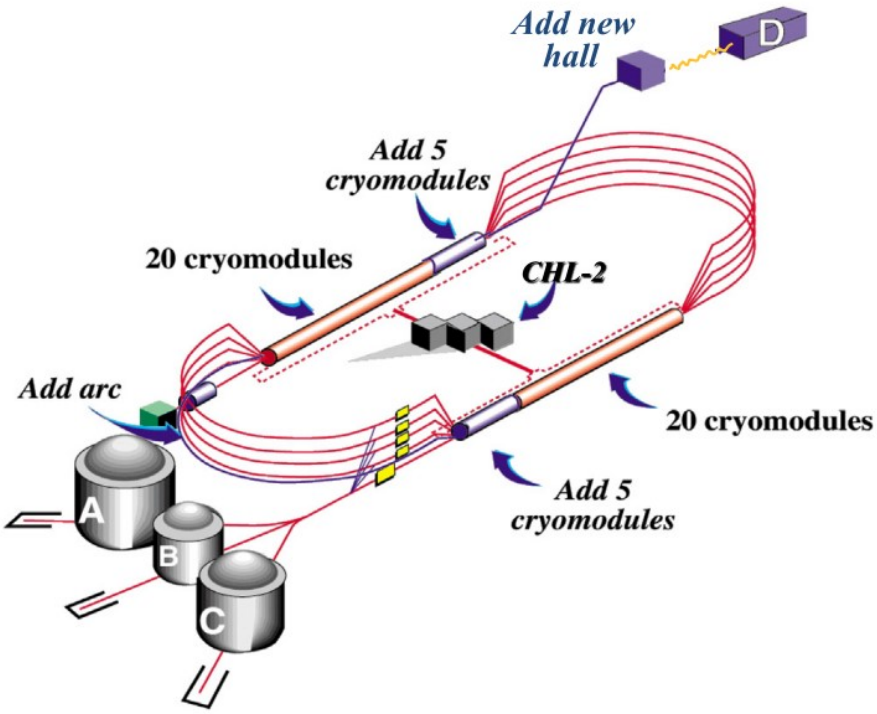

Fig. 2.2 A diagram of the CEBAF accelerator and Halls A, B, C and D at Jefferson Laboratory. The 12 GeV upgrades, such as the new Hall and cryomodules, are shown. [31].

The Continuous Electron Beam Accelerator Facility (CEBAF), Fig. 2.2, is responsible for producing polarised electrons, accelerating them to 12 GeV and then guiding them into the four Halls. Polarised electrons are produced by a multi-kV photogun, this component uses a high-energy laser to free electrons from a GaAs/GaAsP semiconductor device via photo-emission. The emitted electrons have a high average longitudinal polarisation of 85% or greater, this polarisation is maintained in electron beams at currents below 1 mA – the photogun produces electron beams at around 100 µA [29],[30],[32],[33]. Despite its name, the CEBAF accelerator produces bunches of electrons as opposed to a continuous beam, however, this succession of bunches is referred to as the beam. This is accomplished within the photogun by the firing of a pulsed (rather than continuous) laser at the semiconductor. A high pulse frequency results in a high bunch spacing – the time between successive electron bunches. For example, a 499 MHz frequency laser corresponds to a 2 ns bunch spacing, a 249.5 MHz frequency to a 4 ns spacing and a 124.75 MHz frequency to an 8 ns spacing [34].

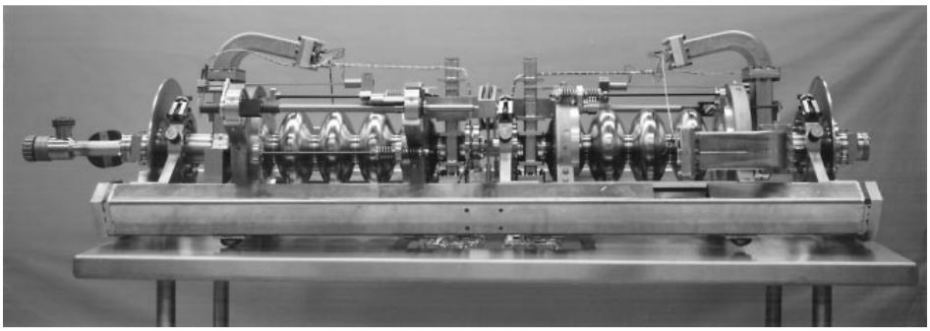

Fig. 2.3 An image of CEBAF cavity pair, i.e. a single cryounit. Four of these pairs form a cryomodule, each LINAC has 25 cryomodules. [29].

Once produced by the photogun, the beam is accelerated as it passes through the 123 MeV injector and into the north linear accelerator (LINAC). The north and south LINACs, identical in design and construction, are each comprised of 25 cryomodules. A single cryomodule is comprised of four cryounits and a single cryounit is comprised of a pair of hermetically joined cavities, Fig. 2.3. The cavity pair is filled with helium gas cooled to around 2 K and accelerates electrons via radiofrequency technology, hence the LINACs are known as superconducting radiofrequency (SRF) LINACs. Of the LINACs 25 crymodules, 20 provide an energy gain of 30 MV to the beam and 5 provide an energy gain of 100 MV to the beam, overall providing an energy of 1.2 GeV to the beam as it passes through the LINAC. Once the beam leaves the north LINAC, it enters a recirculation arc that uses quadrupole

and steering dipole magnets to turn the beam in a 180° arc and send it into the south LINAC. The south LINAC provides 1.2 GeV to the beam which is then circulated back into the north LINAC. This configuration – two antiparallel LINACs joined by recirculation beam lines – is known as a racetrack. The beam circulates four more times, leaving the south LINAC on its fifth and final circulation with an energy of 10.6 GeV. The beam is then split between Halls A, B, C and D [29].

2.3 CLAS12

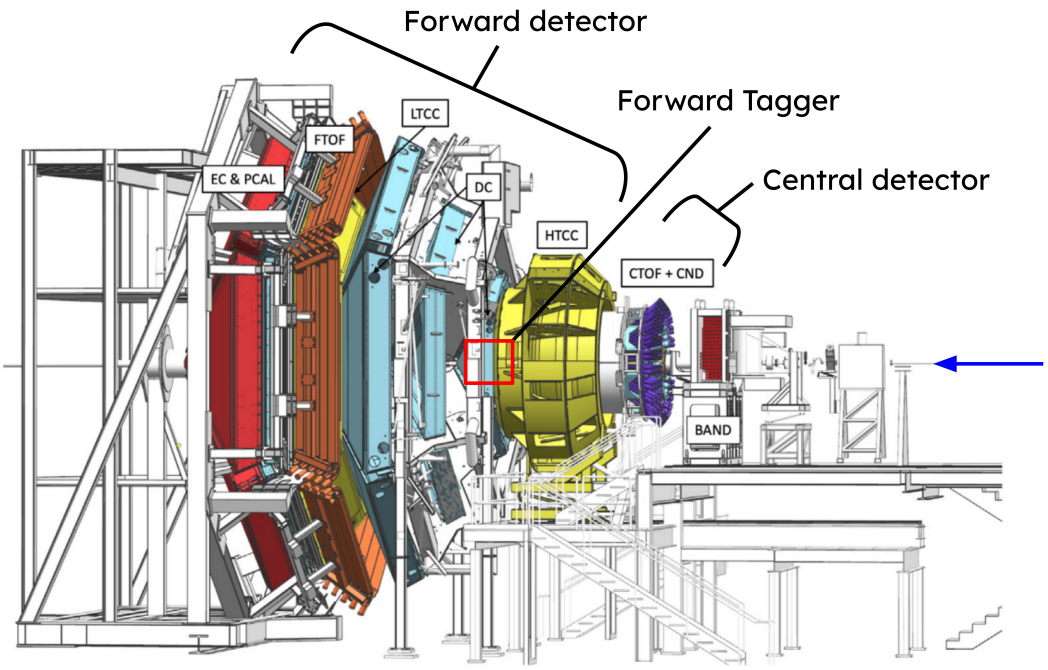

Fig. 2.4 A diagram of the CLAS12 spectrometer. The three detector regions: the Forward Tagger, the Forward Detector and the Central Detector, and important components such as the Forward Time-Of-Flight (FTOF) system and High Threshold Cherenkov Counter (HTCC) are shown. Also shown is a section of the beam pipe (right) that the electron beam enters through from the CEBAF accelerator (not shown). The direction of the electron beam is shown by the dark blue arrow [31].

The CEBAF Large Acceptance Spectrometer operating at 12 GeV (CLAS12), Fig. 2.4, located in Hall B is capable of detecting particles scattered off a fixed target across a wide range of angles. The electron beam produced and accelerated by CEBAF impinges off a fixed target inside CLAS12, resulting in many reactions and the production of various particles that are directly detected or decay

into product particles that are then detected by CLAS12. For the research presented in this thesis, a liquid hydrogen target was used. The CLAS12 detector is comprised of the Forward Tagger, the Forward Detector and the Central Detector [31]. Each of these detector regions and the data acquisition system will be detailed in the following sections.

2.4 The Forward Tagger

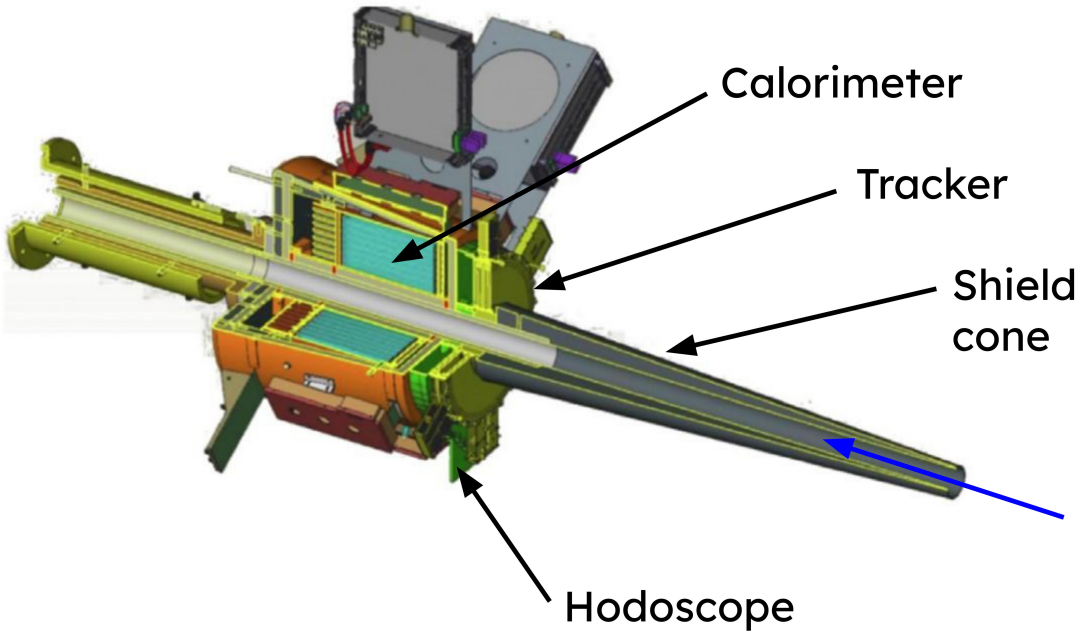

Fig. 2.5 A CAD drawing of the Forward Tagger. The calorimeter (cyan), hodoscope (green) and tracker (yellow) components are shown. Also shown is the tungsten shield that absorbs Moller electrons and the electromagnetic background produced by the beam, preventing it from entering the FT. The direction of the electron beam is shown by the blue arrow [35].

The Forward Tagger (FT) is a component of the CLAS12 spectrometer responsible for detecting low-angle scattered electrons and photons in the forward angle range $2.5^\circ \leq \theta \leq 4.5^\circ$ and azimuthal angle range $0^\circ < \phi < 360^\circ$. It has three main components: the electromagnetic calorimeter (FT-Cal), responsible for identifying electrons and measuring electromagnetic shower energy; the Micromegas trackers (FT-Trk), responsible for measuring charged particle scattering angles; and the scintillation hodoscope (FT-hodo), responsible for separating electrons and high-energy photons.

The FT Calorimeter

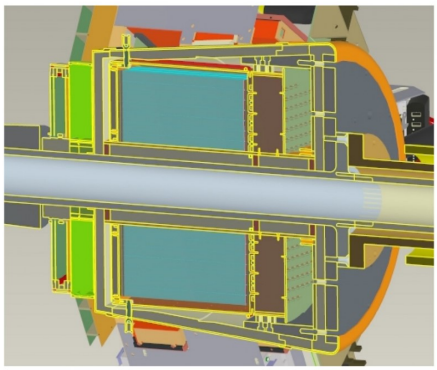

(a) A CAD drawing of the FT Calorimeter

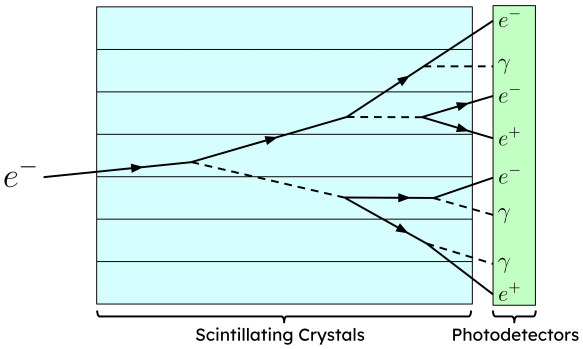

(b) Electromagnetic shower

Fig. 2.6 A CAD drawing of the FT Calorimeter (a) showing the several scintillating crystals (blue) surrounded by the copper shield (orange) and insulating foam (grey) [35]. A diagram of an electromagnetic shower (b) that occurs when an electron enters the scintillating crystals.

The FT-Cal component, Fig. 2.6a, provides information on the energy, position and timing of charged particles. This component is comprised of 332 $15 \times 15 \times 200$ mm^2 $PbWO_4$ (lead-tungstate) crystal scintillators, each weighing 370 g, surrounded by a copper thermal shield and insulating foam. An electron that scatters off the target within the FT forward angle range ($2.5^\circ \leq \theta \leq 4.5^\circ$) passes into the scintillating crystal of the FT and produces an electromagnetic shower – a cascade of electrons, positrons and photons. Showers are produced when electrons interact with the electric field nuclei of atoms that form the scintillating crystal, causing the electron to decelerate and radiate photons. Due to the high energy of the initial electrons, the high-energy radiated photons have sufficient energy to undergo pair production, producing electrons and positrons that go on to produce more photons which go on to produce positrons and electrons via pair production. This process repeats throughout the scintillating crystal to produce an electromagnetic shower. The photons in these showers are detected by semiconductor photodetectors which measure the energy and time of arrival of the charged particle. These measurements are used to determine the identity of the charged particle during event reconstruction [1],[35].

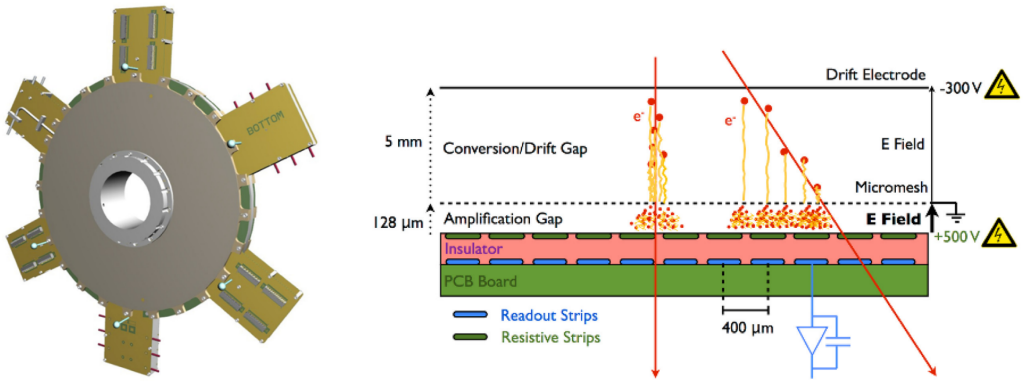

(a) A CAD drawing of the FT Tracker (b) A schematic diagram of a Micromegas tracker

Fig. 2.7 A CAD drawing of the FT Tracker (a) [35]. A schematic diagram of a Micromegas tracker (b) showing how the electrons ionise the gas molecules to produce free electrons that drift to the amplification gap, are amplified and then detected [36].

The FT Tracker

The FT-Trk component provides information on the scattering angle and the trajectory of charged particles. This component is comprised of two double-layers of Micromegas detectors, Fig. 2.7a, which are a type of gaseous detector. A Micromegas detector consists of a 5 mm tall drift gap filled with a gaseous mixture of mostly argon, up to 10% isobutane and up to 5% of CH_4 that sits on a 128 µm amplification region that sits on a PCB board system. An electron that scatters off the target at a low angle passes through the drift gap and ionises the gas molecules which release free electrons that drift to the amplification gap. In the amplification gap, the free electrons are accelerated by a high-voltage electric field and produce electromagnetic showers that are detected by the PCB board system [35], [36].

The FT Hodoscope

The FT-Hodo component provides information that allows the differentiation between electrons and photons that produce electromagnetic showers that are detected in the FT-Cal. This component is comprised of 232 plastic scintillators that are attached to photodetectors and optical fibres responsible for the readout. These scintillators work similarly to the scintillating material in the FT-Cal. Electron

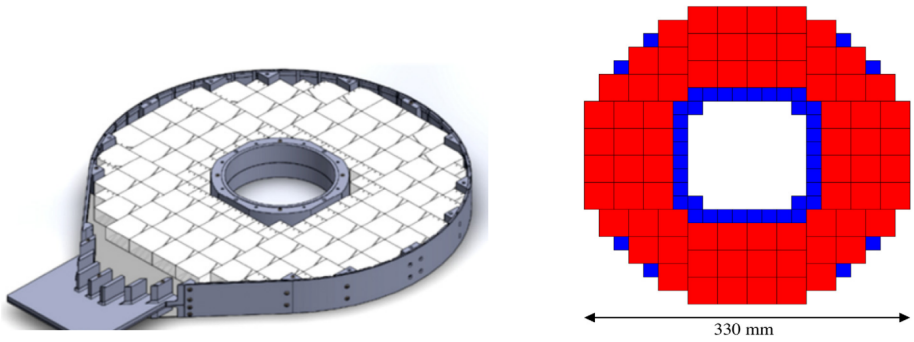

(a) A CAD drawing of FT Hodoscope (b) A diagram of the FT Hodoscope

Fig. 2.8 A CAD drawing (a) and schematic diagram (b) of one of the two layers of plastic scintillators that make up the FT Hodoscope. [35].

and photon showers detected in the FT-Cal can be differentiated by comparing the signal measured in the FT-Cal and FT-Hodo, allowing electrons to be identified [35].

2.5 The Forward Detector

The Forward Detector (FD) consists of various components responsible for providing information on particles scattered off the target up to a forward angle of 35°. Its main components are the High Threshold Cherenkov Counter (HTCC), the Drift Chambers (CD), the Forward Time-Of-Flight (FTOF) system and the Electromagnetic Calorimeters (ECAL). The Drift Chambers provide particle trajectories whilst the High Threshold Cherenkov Counter, Forward Time-Of-Flight system and Electromagnetic Calorimeters work in conjunction to provide particle identification and energy measurements for electrons, protons, photons, kaons, pions and neutrons [31].

The High Threshold Cherenkov Counter

The High Threshold Cherenkov Counter, Fig. 2.9a, is responsible for separating electrons with momenta up to 4.9 GeV from charged pions, kaons and protons in the forward angle range $5^\circ \leq \theta \leq 35^\circ$ and the full azimuthal angle range. The inside of this detector is filled with CO_2 and contains a large, multi-focal mirror, Fig. 2.9b, of 48 mirror facets used to focus Cherenkov radiation onto 48 photomultiplier tubes which produce the output signals. Cherenkov radiation is produced when charged particles travelling in a dispersive medium (CO_2 in the case of the HTCC) at speeds greater

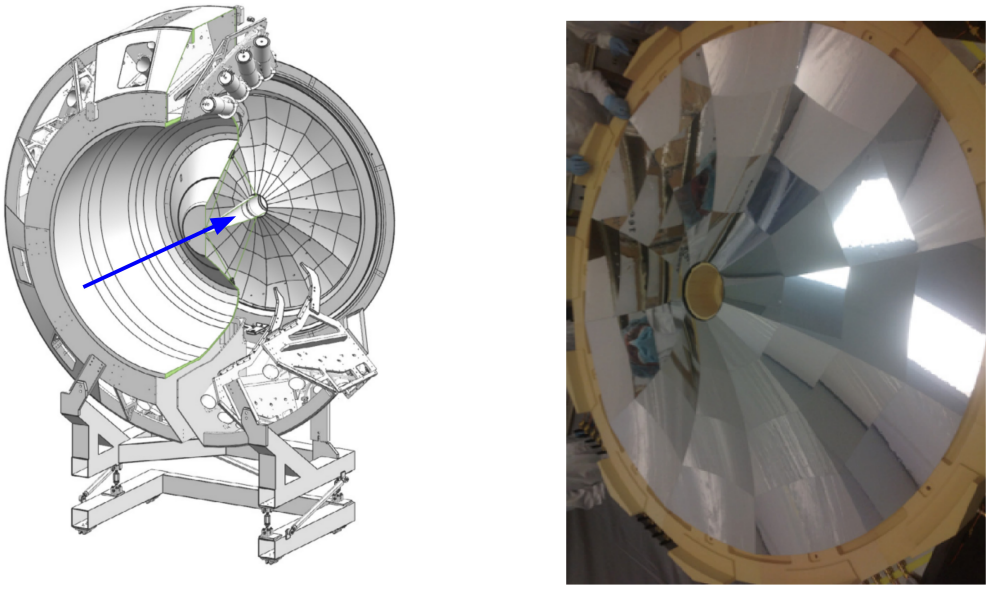

(a) A CAD drawing of the HTCC

(b) A photograph of the HTCC mirror

Fig. 2.9 A CAD drawing of the HTCC (a), the electron beam direction is shown by the dark blue arrow, and a photograph of the HTCC mirror (b) [35].

than that of light in the medium, $v > c/n$ where n is the refractive index of the medium. As these particles traverse the medium, excited atoms near the charged particle become polarised and then lose their excitation energy by emitting coherent radiation at a characteristic angle. This radiation is known as Cherenkov radiation. The HTCC is also used as a trigger for scattered electrons and can be used in conjunction with the Electromagnetic Calorimeters to verify the detection of electrons with specific energies [1],[31].

The Drift Chambers

The Drift Chambers, Fig. 2.10a, are responsible for measuring the momentum, the electric charge and the reconstructed trajectory of a charged particle. The detector is segmented along the beamline into the three regions R1, R2 and R3 (in order of increasing size). Each of these regions is divided azimuthally into six sectors and each of these sectors contains one drift chamber for a total of 36 chambers. Each chamber is filled with argon/CO_2 (90/10 mixture) and has 40-60 sense wires and numerous field wires arranged in two superlayers. The wires in the superlayer are organised in a

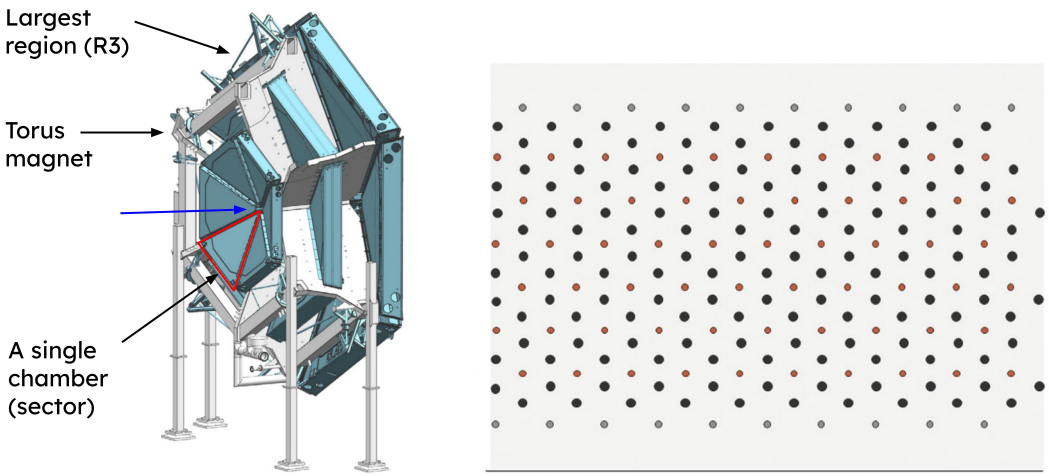

(a) A CAD drawing of the DC system

(b) A diagram of a DC superlayer

Fig. 2.10 A CAD drawing of the DC (a). The largest region (R3), the torus magnet (light grey) and a single R1 chamber (red triangle) are shown [31]. The electron beam direction is shown by the dark blue arrow. A diagram of a DC superlayer (b) perpendicular to the direction of the sense wires, represented by the red dots, and the field wires, represented by the black dots [37].

"brick wall" pattern, as shown in Fig. 2.10b, and produce an electric of strength 50-200 kV throughout the chamber. The three regions are housed in a large structure known as the torus magnet which produces a magnetic field of strength ∼3 Tm. When a charged particle enters the DC system and passes through the chambers, it is curved by the magnetic field of the torus magnet. The amount of curvature allows for the trajectory of the particle to be reconstructed and is directly related to its momentum and charge. As the particle passes through the superlayer it ionises the gas molecules which then drift to the various wires and are detected. Due to the extensive array of wires, the path of the charged particle can be reconstructed by detecting the trail of ions it leaves behind [31],[37], [38]. The concept is similar to the FT Tracker detailed in Sec. 2.4.

The Forward-Time-Of-Flight System

The Forward Time-Of-Flight system, Fig. 2.11a, is responsible for identifying and measuring the time-of-flight of charged particles with momentum up to ∼5 GeV and within the forward angle range $5^\circ \leq \theta \leq 35^\circ$. This detector is divided azimuthally into six regions that each contain sets of high-luminosity scintillating crystals with photomultiplier tubes (PMTs) attached to either end of

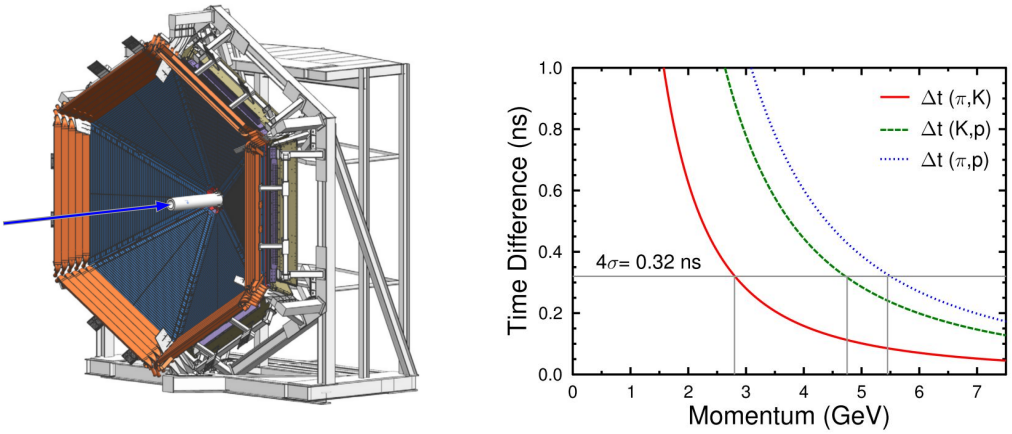

(a) A CAD drawing of the FTOF system

(b) Flight time differences between particles

Fig. 2.11 A CAD drawing of the FTOF system (a) where the electron beam direction is shown by the dark blue arrow [31]. The difference between the TOF of pairs of particles. When the difference falls below 0.32ns, the particles can no longer be identified or distinguished from one another using their TOF [39].

a set of crystals. When a particle passes through the scintillating crystals, atoms are ionised and subsequently release scintillating photons which are detected by the PMTs. By using this detection information, the time-of-flight – the time taken to travel from the interaction point to the detector – of the particles can be calculated to a high precision. The FTOF system identifies which beam bunch a selection of detected particles belonged to by using the time-of-flight of detected electrons, in this case, the electron is known as the trigger particle as it's used for bunch identification. An accurate time-of-flight must be known in order to successfully identify detected particles. The time resolution of the FTOF system is 50 ps at small angles, 200 ps at large angles and about 80 ps on average. The maximum momentum at which particles can be identified correctly, known as the momentum threshold, is given at 4σ for the FTOF system. The ability of the FTOF system to separate particles by their time-of-flight is dependent on their momentum. This dependence is shown graphically in Fig. 2.11b where the 4σ threshold corresponds to the threshold time difference between charged particles. For the FTOF system, the limit for π/K separation is 2.8 GeV, K/p separation is 4.8 GeV and π/p separation is 5.4 GeV [31],[39].

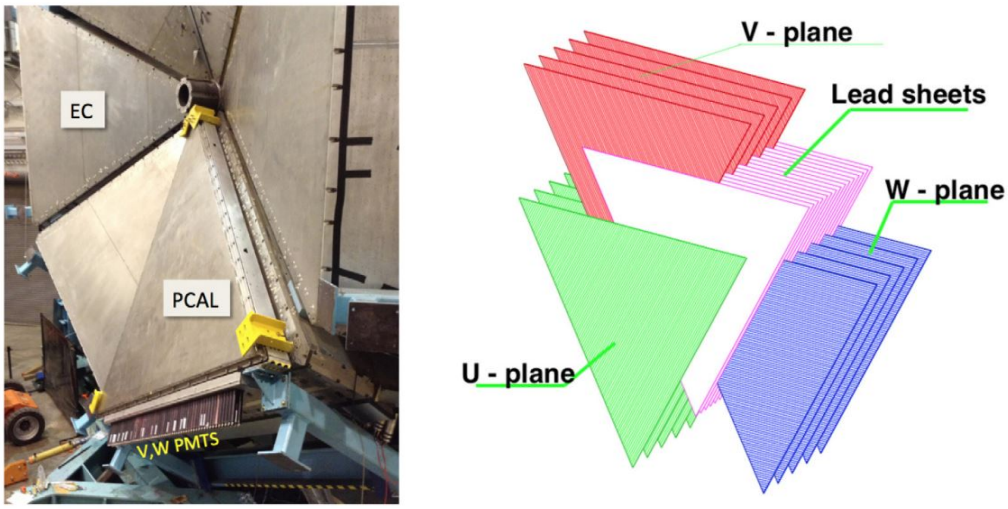

(a) A photograph of the ECAL (b) A diagram of the ECAL layer design

Fig. 2.12 A photograph of the ECAL (a) where a PCAL module is shown in front of the EC modules, the PMTs are also shown [40]. A diagram of the ECAL layer design (b) showing the interwoven scintillating and lead layers for the different planes [40].

The Electromagnetic Calorimeter

The Electromagnetic calorimeters, Fig. 2.12a, comprised of the pre-shower calorimeter (PCAL) and the electromagnetic calorimeter (EC), are responsible for identifying electrons (up to 12 GeV), photons (mainly from hadronic decays, e.g. $\pi_0 \rightarrow \gamma\gamma$) and neutrons in the forward angle range $5^\circ \leq \theta \leq 35^\circ$. This detector is divided azimuthally into six equal modules which are each made of a PCAL layer in front of an EC layer. A module has 54 1-cm-thick scintillating layers, 15 in the PCAL and 39 in the EC, that are interwoven between 2.2-mm-thick sheets of lead, as seen in Fig. 2.12b. PMTs are attached to the sides of these modules and are responsible for detecting and measuring the energy the scintillating light produces when charged particles pass through the scintillating crystals. A module has three planes: U, W, and V. These planes refer to the different readout planes resulting from the different orientations of the scintillating strips that comprise the scintillating layers. For example, the W-plane strip orientation, and therefore the readout plane, are parallel to the U PMT readout side. The entire ECAL system has a thickness of 20.5 radiation lengths which is sufficient to fully absorb an electromagnetic shower meaning that the total energy deposited by a detected particle is measured. A particle-induced shower is identified using a cluster reconstruction algorithm and a shower above

a certain energy is known as a hit in the calorimeter. The position of a hit is determined to a high resolution by comparing measurements of the same hit taken by the PCAL and the EC [40].

2.6 The Central Detector

The Central Detector (CD) provides information on particles scattered off the target in the forward angle range $35^\circ \leq \theta \leq 125^\circ$ and azimuthal angle range $0^\circ < \phi < 360^\circ$. Its main components are the Central Vertex Tracker (CVT), the Central Time-Of-Flight (CTOF) system and two neutron detectors.

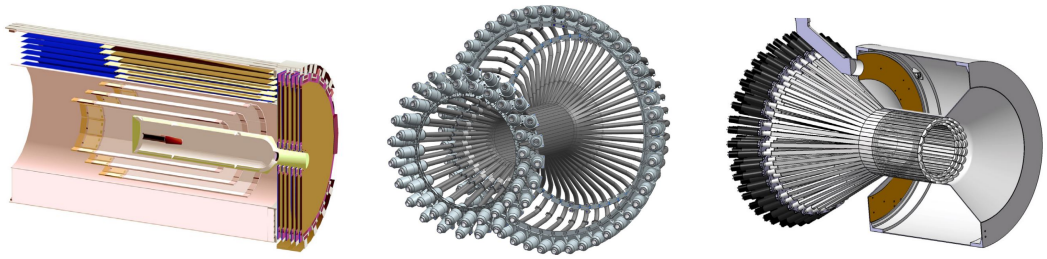

(a) The CVT (b) The CTOF (c) The CND

Fig. 2.13 CAD drawings of the Central Detector CVT (a), CTOF detector (b) and CND (c).

The Central Vertex Tracker, 2.13a, is responsible for measuring momentum and determining the vertex of charged particles in the CD forward angle region. This component is comprised of a Silicon Vertex Tracker (SVT) and a Barrel Micromegas Tracker (BMT). The former consists of 32 double-sided modules of silicon sensors connected to a readout system and the latter of six layers of cylindrical Micromegas gas trackers. The Forward Micromegas Tracker (FMT), consisting of 6 Micromegas disks, is another important component of the CVT but covers the forward angle region $5^\circ \leq \theta \leq 35^\circ$ [31],[36].

The Central Time-Of-Flight system, 2.13b, identifies charged particles in the momentum range 0.3-1.25 GeV and CD forward angle region via time-of-flight measurements. This component consists of 48 plastic scintillators connected to readout PMTs by light guides. The CTOF system surrounds the target and CVT, and provides a time-resolution of 80 ps for TOF measurements used for charged particle identification [31].

The neutron detectors consist of the Central Neutron Detector (CND), 2.13c, and the Back Angle Neutron Detector (BAND). The CND detects neutrons in the momentum range 0.2-1.0 GeV and CD forward angle region by use of 144 scintillator paddles split evenly across three layers and connected to

PMTs. The BAND detects backward neutrons in the momentum range 0.25-0.7 GeV and $155^\circ - 175^\circ$ forward angle region by using 18 rows and 5 layers of scintillator bars connected to PMTs [31].

2.7 The Data Acquisition System

The CLAS12 data acquisition (DAQ) system is responsible for collecting and processing data from the CLAS12 detector. Some important capabilities include reconstructing events, data quality monitoring, implementation of the trigger system and recording data to tape.

The system continually monitors the quality of data during experiments by sampling and analysing a small number of events, allowing for actions to be easily taken if needed. Events are reconstructed using reconstruction algorithms. The entire system is connected by high two 40 Gb uplinks to the JLab computer centre where data are permanently stored onto tapes.

Data Flow and Hardware

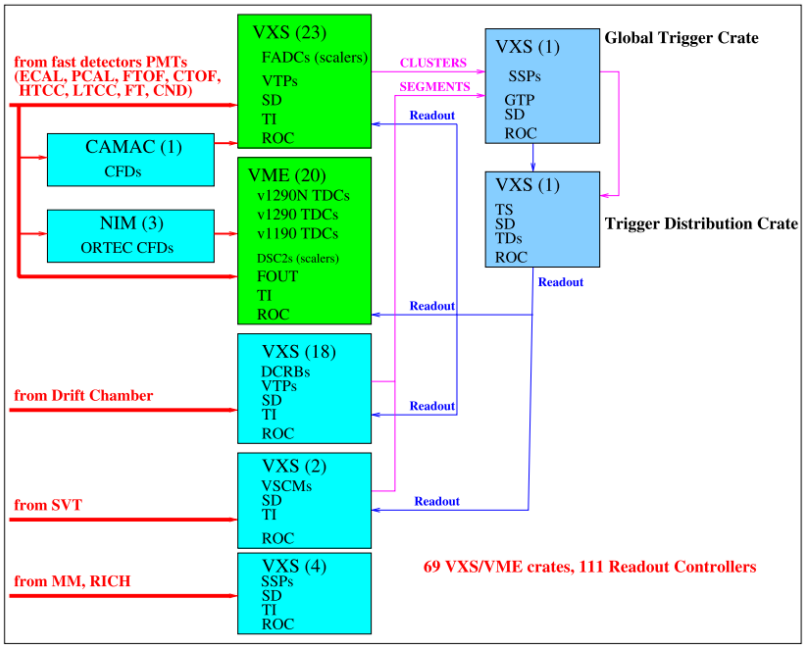

Fig. 2.14 A schematic diagram of the data accusation and trigger system. The flow of data from the detector components and into the VXS crates and VTPs is shown by the red arrows[31].

The DAQ system is designed to operate continuously at a desired average trigger rate of 20 kHz and 200 MB/s data rate. Data from CLAS12 are passed into the DAQ system processing. The data-

taking process begins in the front-end components known as Readout Controllers (ROCs) consisting of commercial and custom VME/VXS crates, Linux servers and JLab-designed VXS Trigger Processor boards (VTPs). A diagram of the DAQ system, including important components, is shown in Fig. 2.14.

Triggers and Event Reconstruction

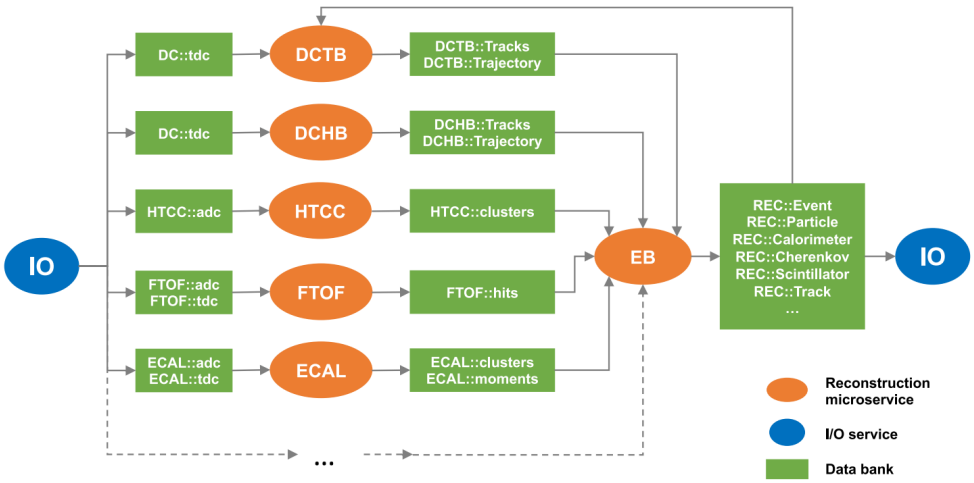

Fig. 2.15 A schematic diagram of the event reconstruction process. Data are passed into the system by the I/O (input/output) service, then organised into banks (green) and processed by the reconstruction services (orange). The Event Builder (EB) and final output banks (green, rightmost) are also shown [41].

Event reconstruction and the implementation of triggers are important techniques in the analysis of the huge amount of data produced by CLAS12. A trigger is a condition set during the production and collection of data which restricts the types and number of particles collected. Most of the experiments conducted using CLAS12 require information on the scattered electron, therefore a trigger must be imposed on the electron. This trigger requires that the scattered electron must be detected by multiple detector components and above a certain energy by the electromagnetic calorimeters.

Event reconstruction involves combining momentum and velocity to obtain the mass of a detected particle. Additionally, independent measurements of momentum and velocity are compared to ensure the mass and therefore the identity of the particle are correct. A diagrammatic representation of the event reconstruction process is shown in Fig. 2.15. During the process, data are stored in banks and processed using reconstruction services and the Event Builder (EB). The final output banks contain information on events and individual particles such as momentum or detector response. These banks

are stored in High-Performance Output (HIPO) files which can be read using ROOT frameworks [31],[41].

Chapter 3

Data Analysis

This chapter describes the data analysis techniques used to study the CLAS12 data. The chapter ends with a discussion of the simulations used in this research. The data used in this analysis was produced at CLAS12 in the Spring of 2019 as a part of Run Group A (RG-A). RG-A used a liquid hydrogen target. Recently, this data has been recalibrated, meaning that novel results can be obtained once a comprehensive analysis has been completed.

3.1 Event Selection

The analysis of the data began with the process of selecting the correct events. An event is defined as the interaction between an incoming electron and the target, resulting in a group of outgoing particles known as the final state. The properties of the particles in the final state can be used to reconstruct the event in order to investigate the types of resonances that may have been produced. The final state analysed in this research consists of an electron, a proton, a positive kaon and a negative kaon, and is labelled epK^+K^-. This final state is used to investigate reactions involving meson photoproduction such as the one shown in Fig. 1.6. During data collection, the trigger was configured to require hadrons to be detected by the forward detector and electrons to be detected by the Forward Tagger with a detected energy of less than 5.5 GeV.

3.1.1 Topology

A topology is a set of detected particles used to describe a final state associated with the reaction of interest. There may be many possible topologies associated with a single final state. Topologies

are classified as exclusive or inclusive, the former requires all the particles in the final state to be detected and the latter requires for only some of the particles in the final state to be detected. An event identified using an inclusive topology must correspond to the desired final state; therefore, it must be ensured that the particles missing from this event were indeed produced. The process of identifying the missing particles is related to reaction reconstruction which will be detailed in Sec. 3.2.

Selecting events based on topology is the most rudimentary type of event selection and was the first method employed with the use of a software package known as chanser (which stands for CLAS12 HIPO Analyser) [42]. Four topologies were chosen: one exclusive, epK^+K^-; and three inclusive, eK^+K^-, epK^- and epK^+. The exclusive topologies require all four particles to be detected whilst the three inclusive topologies each allow for a missing particle. Before reaction reconstruction, the identities of individual particles must be verified. The CLAS12 Event Builder (EB) is responsible for Particle Identification (PID). The accuracy of this identification process is limited by properties of the detector such as momentum and timing resolution. Thus, particle identification must be improved by constraining the properties of the particles calculated by the EB.

3.1.2 β and χ^2_{PID}

The mass of a particle is unique to its species. Therefore, if the species of a particle has been identified correctly then it should have a mass equal to the mass associated with that species. The particle species provided by the EB can be verified by using the mass and another quantity known as the relativistic speed of the particle, denoted β. Two independent measurements β were compared to ensure the EB identified particles correctly.

The first independent value of β was calculated by the Event Builder using time-of-flight information during event reconstruction. Due to the trigger, the TOF of protons and kaons were measured using the FTOF detector and the TOF of electrons using the Forward Tagger. β_{TOF} is given by

$$\beta_{TOF} = \frac{v}{c} = \frac{d}{ct}, \tag{3.1}$$

where v is the particle's speed, c is the speed of light in a vacuum, d is the distance between the target and the point detection on the detectors, and t is the TOF measured by the detectors. Uncertainty in β_{TOF} is due to the accuracy of the TOF measurement which is dependent on the timing and position resolution of the detectors. The second independent value of β was calculated in this research using

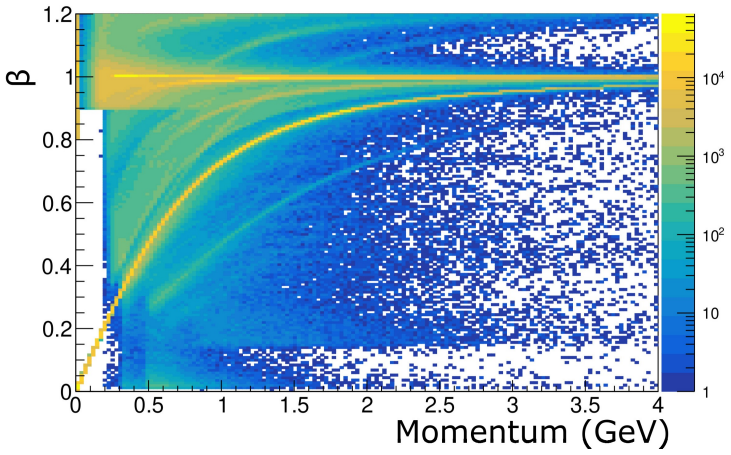

(a) Plot of β as a function of momentum

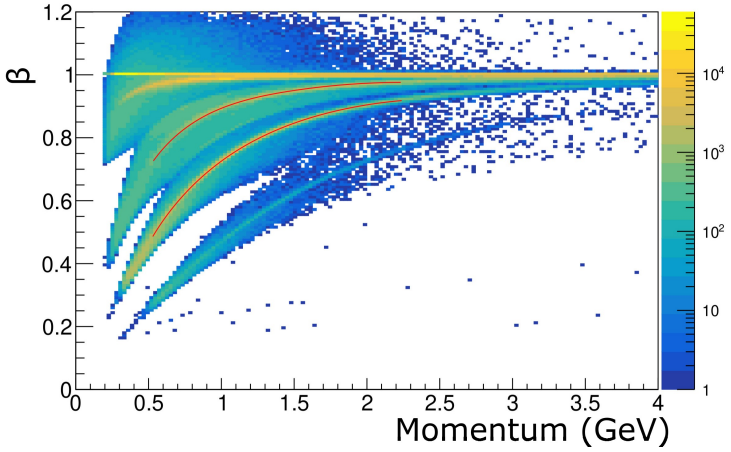

(b) Plot of β with a $|\chi^2_{PID}| < 3.5$ cut

Fig. 3.1 Plots of β as a function of momentum for detected particles including particles that the EB identified as an electron, a proton and a K^+ before (a) and after (b) a $|\chi^2_{PID}| < 3.5$ cut was imposed. Data from 9 Pass2 runs from RG-A spring 2019 were used to produce these plots.

an assumed mass and DC momentum information. β_{DC} is given by

$$\beta_{DC} = \frac{p}{E} = \frac{p}{\sqrt{m^2 + p^2}}, \tag{3.2}$$

where p is the particle momentum measured by the DC system, E is the particle energy and m is the particle species returned by the EB.

If the EB has identified a particle correctly then β_{TOF} and β_{DC} should be comparable since m in β_{DC} is provided by the EB. These values will not be equivalent due to the uncertainty in t due to the FTOF detector timing resolution and the uncertainty in P due to the DC momentum resolution. In

Fig. 3.1a, β_{TOF} is plotted as a function of the magnitude of the particle's momentum for detected particles including the electron, proton and K^+. The red lines show the theoretical value of beta using Eq. (3.2) for the kaon and proton mass. The particles with β_{DC} near this line have likely been

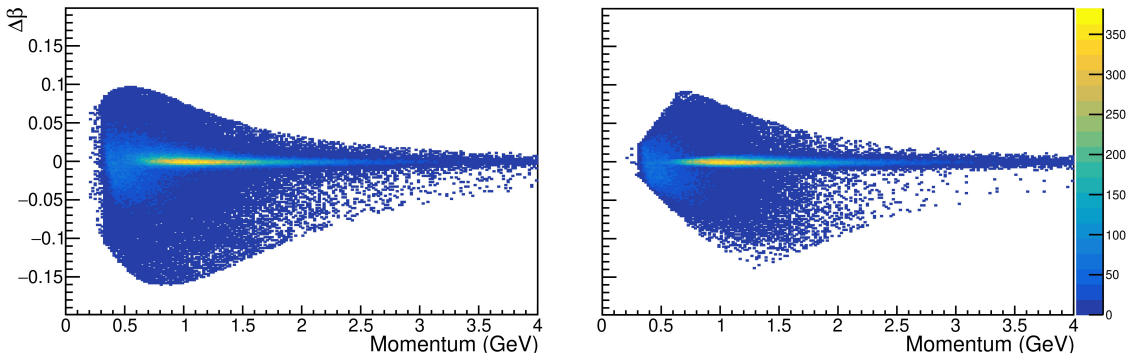

(a) $\Delta\beta$ plots for particles that the EB identified as a proton

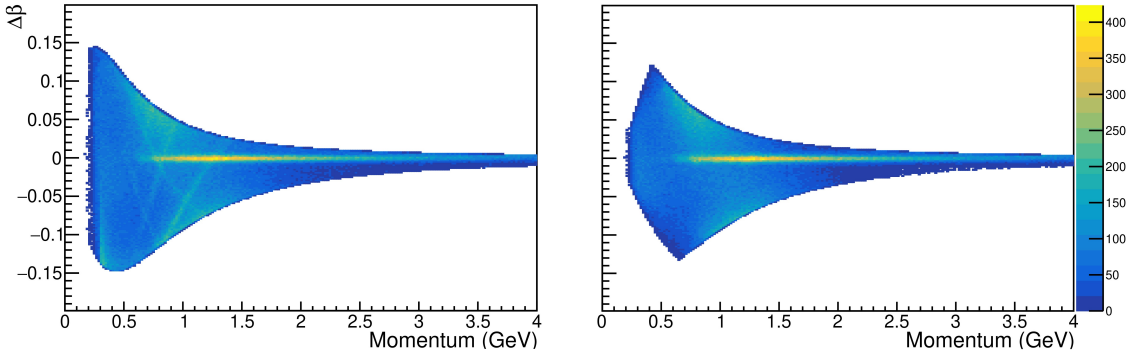

(b) $\Delta\beta$ plots for particles that the EB identified as a K^+

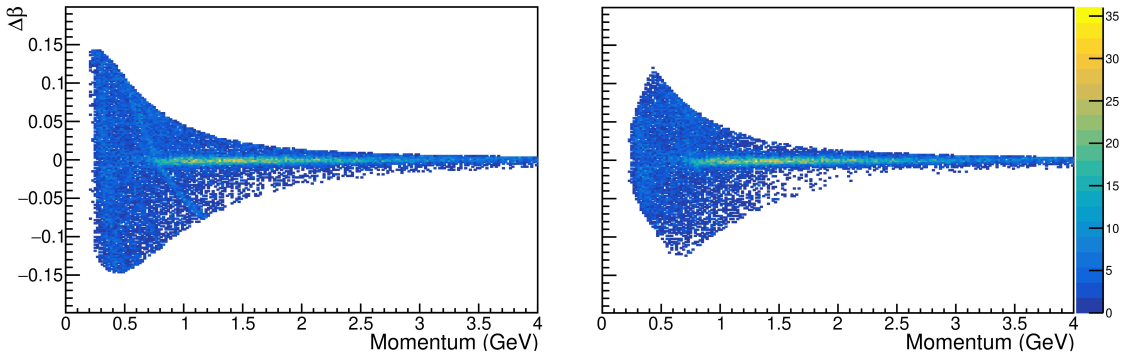

(c) $\Delta\beta$ plots for particles that the EB identified as a K^-

Fig. 3.2 Plots of $\Delta\beta$ as a function of momentum for particles that the EB identified as a proton (a), K^+ (b) and K^- (c) before (left column) and after (right column) a $|\chi^2_{PID}| < 3.5$ cut was imposed. Data shown are from 9 Pass2 runs from RG-A spring 2019.

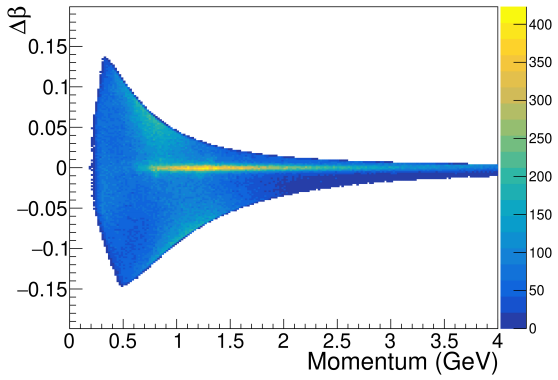

(a) $\Delta\beta$ plot when $|\chi^2_{PID}| < 5.5$

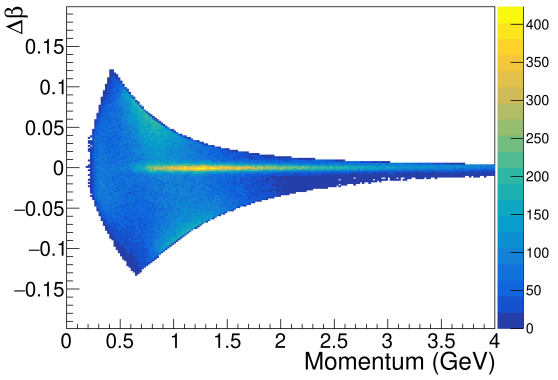

(b) $\Delta\beta$ plot when $|\chi^2_{PID}| < 3.5$

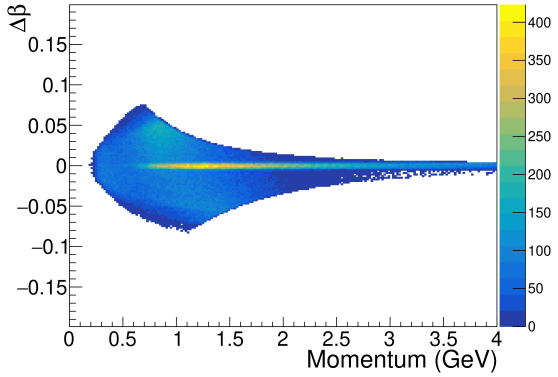

(c) $\Delta\beta$ plot when $|\chi^2_{PID}| < 1.5$

Fig. 3.3 Plots of $\Delta\beta$ as a function of momentum for particles that the EB identified as a K^+ after imposing a $|\chi^2_{PID}| < 5.5$ cut (a), a $|\chi^2_{PID}| < 3.5$ cut (b) and a $|\chi^2_{PID}| < 5.5$ cut (c).

identified correctly since both independent values of beta are in close agreement. In this plot, artefacts corresponding to misidentified particles are seen. For example, particles with $\beta_{DC} > 1$ are unphysical as this implies $v > c$; they may be associated with events from a different beam bunch.

The similarity between β_{TOF} and β_{DC} was quantified using two quantities: $\Delta\beta$ and χ^2_{PID}. $\Delta\beta$ is given by

$$\Delta\beta = \beta_{TOF} - \beta_{DC}, \tag{3.3}$$

and was calculated in this research. χ^2_{PID} is the number of standard deviations that separate β_{TOF} and β_{DC}, and was calculated by the EB. If an event consists of at least one particle with significantly different values of β_{TOF} and β_{DC} then the entire event was disregarded by constraining χ^2_{PID} for each particle.

Imposing this constraint is known as making a χ^2_{PID} cut on the data. To produce Fig. 3.1b, a cut of $|\chi^2_{PID}| < 3.5$ was imposed on the data shown in Fig. 3.1a, resulting in the removal of many unphysical and misidentified particles. The same χ^2_{PID} cut was imposed on the $\Delta\beta$ of the proton, K^+ and K^- as shown in Fig. 3.2. In Fig. 3.2b and Fig. 3.2c, the curved bands passing through $\Delta\beta = 0$ are particles, such as pions, that have been misidentified by the EB as kaons. Once a χ^2_{PID} cut was made, these events were removed. The $|\chi^2_{PID}$ cut was varied and the effect on the $\Delta\beta$ of particles identified as a K^+ was observed as seen in Fig. 3.3. A cut of $|\chi^2_{PID}| < 3.5$ was used in this research to remove unwanted events whilst maintaining a large number of statistics.

3.1.3 TOF and Δt

Constraining the difference between two independent values of the TOF of a particle was also used to reduce the error in particle identification. The first independent value of the TOF is a measurement of the TOF taken by the FTOF detector (FT for electrons) and is hence denoted as t_{TOF}. The second independent value of the TOF is calculated using the momentum measured by the DC system and is hence denoted as t_{DC}. Eq. (3.1) can be rearranged to obtain an equation for t_{DC}, which is,

$$t_{DC} = \frac{d}{c\beta_{DC}}. \tag{3.4}$$

Similarly, as for the two values for β, these two independent values of the TOF should be comparable. A new quantity Δt was defined and is given by,

$$\Delta t = t_{TOF} - t_{DC}. \tag{3.5}$$

The Δt for particles that the EB identifies as an electron, a proton, a K^+ or a K^- are plotted in Fig. 3.4a. The skewed peak for the electron occurs because a pion is used as the start time for the electron when calculating Δt. In addition to the $|\chi^2_{PID}| < 3.5$ cut, a cut of $|\Delta t| < 0.5$ was made in order to reject unwanted events, the result on β_{TOF} is shown in Fig. 3.4b.

3.1.4 Scattered Electron

In the reaction of interest, an electron scatters off the proton target at a low angle via a low Q^2 photon. The energy and angle of the scattered electron can be used to determine the energy, E_γ, polarisation, P

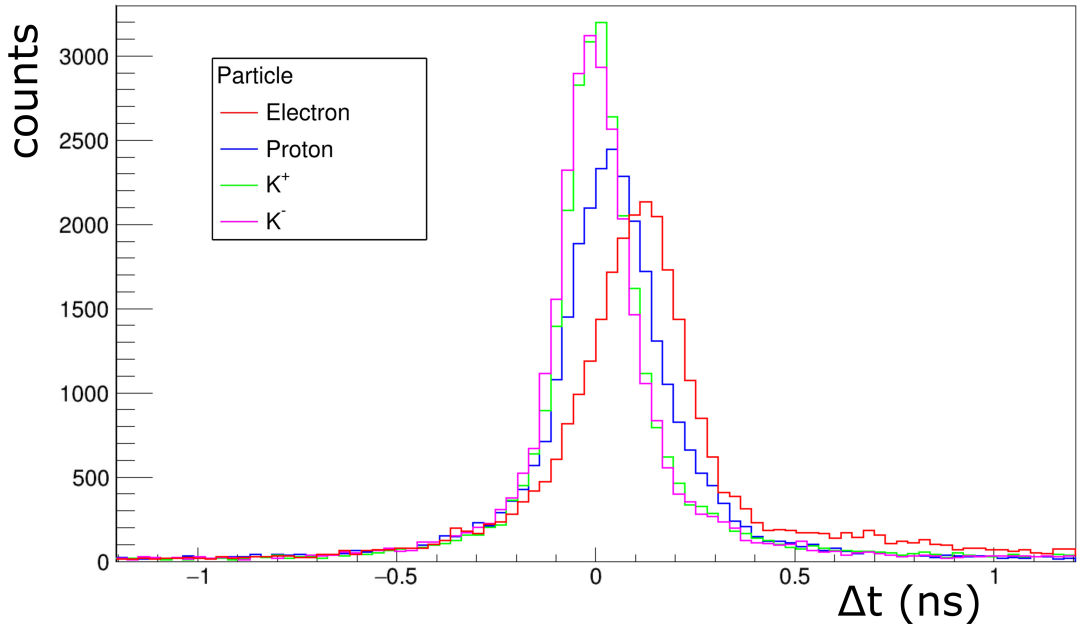

(a) Δt for different particles

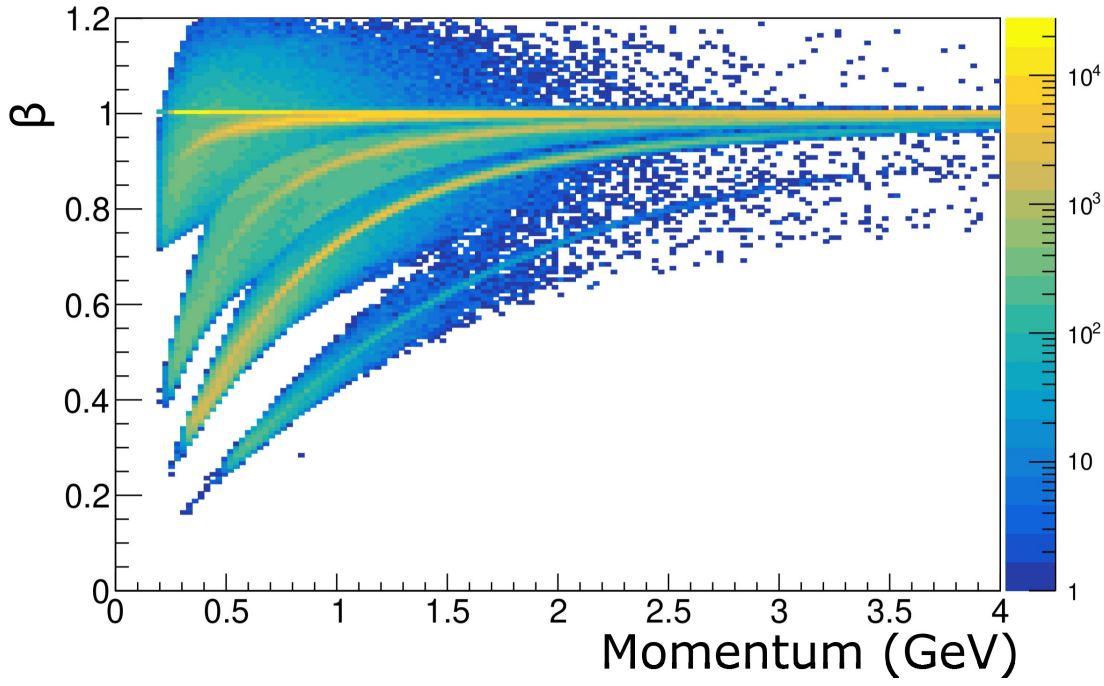

(b) Plot of β as a function of momentum

Fig. 3.4 A plot of Δt (a) for particles that the EB identifies as an electron, a proton, a K^+ or a K^-. A plot of β as a function of momentum (b) for particles that the EB identified as an electron, proton and K^+ after a $|\chi^2_{PID}| < 3.5$ cut and a $|\Delta t| < 0.5$ cut were imposed.

and Q^2 of the photon. For the RG-A Spring 2019 runs, the beam energy used is known to be 10.2 GeV.

The photon energy is given by,

$$\nu = E_b - E_{e'}, \tag{3.6}$$

where E_b is the energy of the beam and $E_{e'}$ is the energy of the scattered electron. The photon Q^2 is given by,

$$Q^2 = 4E_bE_{e'}\sin^2(\frac{\theta_{e'}}{2}), \tag{3.7}$$

where $\theta_{e'}$ is the angle of the scattered electron relative to the beamline. The photon polarisation is given by,

$$P = [1 + 2\frac{Q^2+\nu^2}{Q^2}\tan^2(\frac{\theta_{e'}}{2})]^{-1}. \tag{3.8}$$

This polarisation information is vital as it can be used to understand the angular distribution of the decay products of the meson produced in an electron-target interaction. The low Q^2 information ensures that only low Q^2 photos are selected, corresponding to high polarisation.

To ensure the electron scatters at a low angle, events were selected in which the electron was detected by the Forward Tagger, restricting the electron to an angular range of $2.5^\circ \leq \theta \leq 4.5^\circ$. An additional cut was made to remove electrons with $\theta < 2.0^\circ$ or $\theta > 5.0^\circ$ in the case that the angle had been reconstructed incorrectly by the Forward Tagger. Another important cut imposed on the scattered electron was a cut on its energy. The cut used was $0.4 < E_{e'} < 5.0$ GeV which ensured electrons transferred at least 5 GeV of their energy to the target during an electron-target interaction, allowing for resonances to be produced. This cut also ensured that the real and simulated data were closely matched, which will be elaborated on in 3.3. The result of these cuts on the photon energy, polarisation, and Q^2 are shown in Fig. 3.5.

3.2 Reaction Reconstruction

The events that are selected using the particle identification verification techniques discussed in Sec. 3.1 may still not correspond to the reaction of interest. Reaction reconstruction is required to ensure that selected events do not come from different reactions by considering the properties of all of the particles that make up the event.

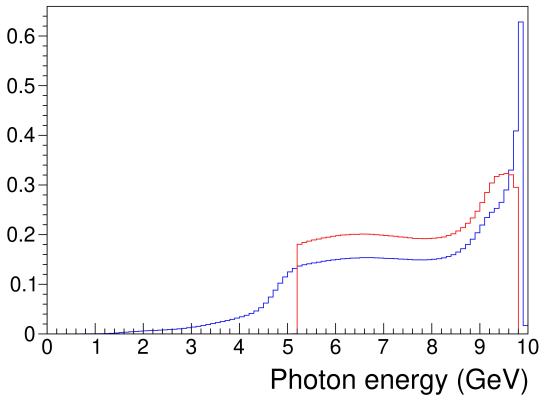

(a) Photon energy

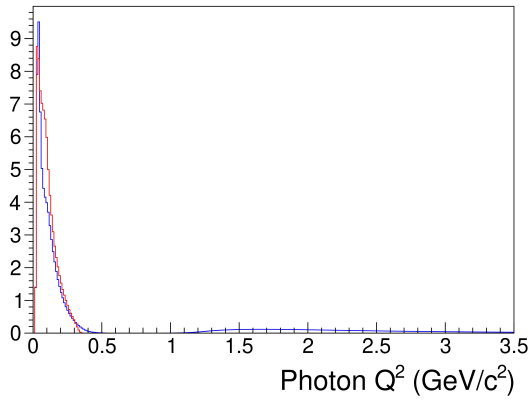

(b) Photon Q^2

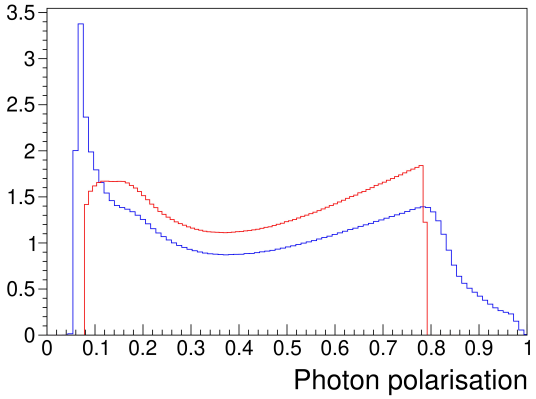

(c) Photon polarisation

Fig. 3.5 Photon energy (a), Q^2 (b) and polarisation (c) before (blue) and after (red) $\theta < 2.0^\circ$ or $\theta > 5.0^\circ$ and $0.4 < E_e < 5.0$ GeV cuts on the scattered electron. All histograms are normalised in a manner which distinguishes the distributions before and after the cuts are made, the y-axis is arbitrary.

3.2.1 Background

Once events have been selected based on the final state particles, there may be some events that correspond to reactions that are not the reaction of interest. These events are referred to as the background, desired events are referred to as the signal. For example, if the CLAS12 detector fails to detect the pion in the reaction $ep \rightarrow e'pK^+K^-\pi^0$ then it would misidentify this event as the desired final state, epK^+K^-, which would contribute to the background. Another example of a background event may be an event that has incorrectly been assigned additional particles from other events. Two properties known as the missing mass squared and the missing mass of an event can be used to check if an event corresponds to the background or signal.

3.2.2 Missing Mass Plots

The missing mass is used to compare the four-momentum of the initial and final state particles in order to reconstruct any undetected particles. The four-momentum of a particle is a four-vector given by

$$P = (E, p_x, p_y, p_z), \tag{3.9}$$

where E is the particle energy, p_x is the momentum in the x direction, p_y is the momentum in the y direction, and p_z is the momentum in the z direction.

The missing mass squared can be calculated for the reaction of interest; in this case, an electron from the beam, e, and a proton from the target, p, are considered as the initial particles. The missing mass squared for $ep \to e'pK^+K^-$ is given by

$$\begin{aligned} MM^2(ep \to e'pK^+K^-X) &= |P_b + P_t|^2 - |P_{e'} + P_p + P_{K^+} + P_{K^-}|^2 \\ &= (E_b + m_t - E_{e'} - E_p - E_{K^+} - E_{K^-})^2 \\ &\quad - |\bar{p}_b - \bar{p}'_e - \bar{p}_p - \bar{p}_{K^+} - \bar{p}_{K^-}|^2, \end{aligned} \tag{3.10}$$

where P_b is the four-momentum of the electron beam, P_t is the four-momentum of the target and $\bar{p}$ is the magnitude of the three-momentum of the respective particle. In Eq. (3.10), X represents the particle that the missing mass squared is being calculated for. Although in the final state there should be no other particles, it's still useful to include X in the calculations. In this thesis, natural units are used meaning that $c = 1$ and masses such as MeV/c^2 and $(GeV/c^2)^2$ are given as MeV and GeV^2. The $MM^2(ep \to e'pK^+K^-X)$ between -0.025 and 0.025 GeV^2 is shown in Fig. 3.6.

The conservation of the four-momentum implies that for the reaction $ep \to e'pK^+K^-$ the magnitude of the four-momentum of the initial state particles should be equal to the magnitude of the four-momentum of the final state particles. This means that $MM^2(ep \to e'pK^+K^-X) = 0\ GeV^2$ for events corresponding to the reaction of interest. If the event has additional particles then $MM^2(ep \to e'pK^+K^-X)$ will deviate from zero. For example, including an undetected pion in Eq. (3.10) increases $MM^2(ep \to e'pK^+K^-X)$ by the square of the mass of the pion, approximately 0.02 GeV^2. To remove these types of background contributions, a cut of $|MM^2(ep \to e'pK^+K^-X)| < 0.01 GeV^2$ was imposed. The result of the $MM^2(ep \to e'pK^+K^-X)$ cut is shown in Fig. 3.6b. A large amount of the background is removed whilst the signal is preserved.

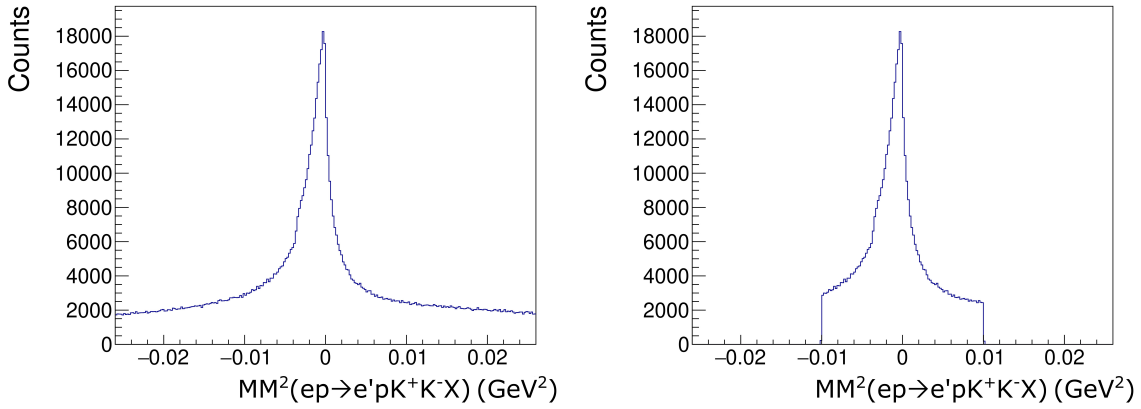

(a) $MM^2(ep \to e'pK^+K^-X)$ (b) $MM^2(ep \to e'pK^+K^-X)$ with cut

Fig. 3.6 $MM^2(ep \to e'pK^+K^-X)$ before (a) and after (b) $|MM^2(ep \to e'pK^+K^-X)| < 0.01\ GeV^2$.

The missing mass was also used to ensure that specific particles were detected whilst removing the background. Since the $e'pK^+K^-$ final state was required, the identity of the particle that was identified as a proton was verified by using the missing proton mass given by,

$$\begin{aligned} MM(ep \to e'K^+K^-X) &= \sqrt{|P_b + P_t|^2 - |P_{e'} + P_{K^+} + P_{K^-}|^2} \\ &= \sqrt{(E_b + m_t - E_{e'} - E_{K^+} - E_{K^-})^2 - |\bar{p}_b - \bar{p}_{e'} - \bar{p}_{K^+} - \bar{p}_{K^-}|^2}. \end{aligned} \tag{3.11}$$

If the $e'pK^+K^-$ final state has been identified correctly then $MM(ep \to e'K^+K^-X) = m_p$. A plot $MM(ep \to e'K^+K^-X)$ between 0.5 and 1.3 GeV is shown in Fig. 3.7a.

A cut of $0.7 < MM(ep \to e'K^+K^-X) < 1.1$ was imposed on $MM(ep \to e'K^+K^-X)$. This range was chosen so that events were selected that lie within the signal peak and so that the background was removed, as shown in Fig. 3.7a. The missing mass of the particles in the same event are correlated; therefore, a cut imposed on one particle affects all particles. The result of the $MM(ep \to e'K^+K^-X)$ cut on the missing mass of $ep \to e'pK^-X$, $MM(ep \to e'pK^-X)$, and of $ep \to e'pK^+X$, $MM(ep \to e'pK^+X)$, is shown in Fig. 3.7b and Fig. 3.7c. After the $MM(ep \to e'K^+K^-X)$ cut was imposed, background events for $MM(ep \to e'pK^-X)$ and $MM(ep \to e'pK^+X)$ are reduced. The peak for each missing mass corresponds to the mass of the missing particle as expected. Effects such as timing and momentum resolution of the detectors introduce uncertainty into the missing mass, making them partly responsible for the widths of the mass peaks.

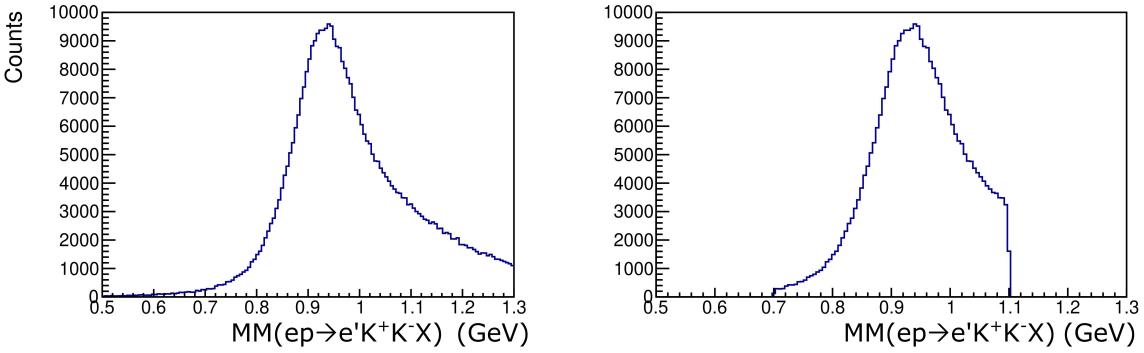

(a) $MM(ep \to e'K^+K^-X)$ before (left) and after (right) $0.7 < MM(ep \to e'K^+K^-X) < 1.1$ GeV cut

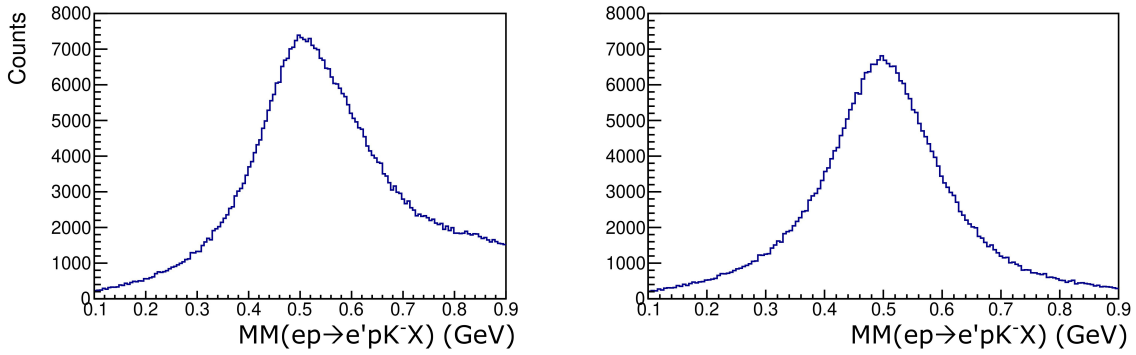

(b) $MM(ep \to e'pK^-X)$ before (left) and after (right) $0.7 < MM(ep \to e'K^+K^-X) < 1.1$ GeV cut

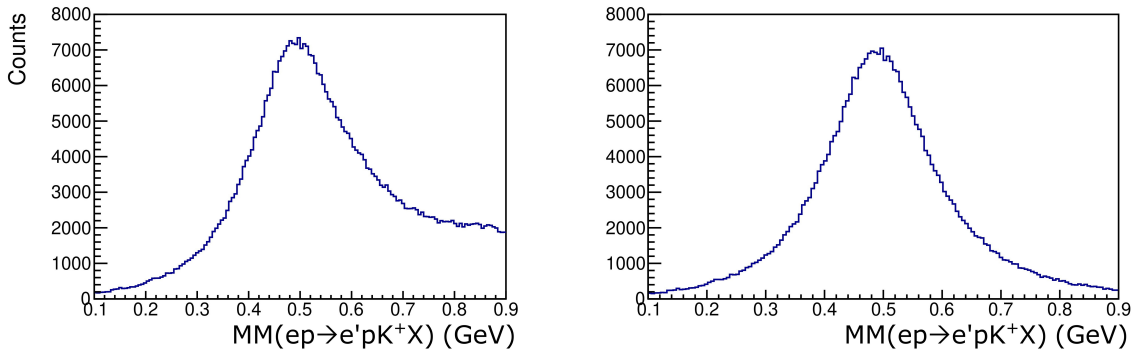

(c) $MM(ep \to e'pK^+X)$ before (left) and after (right) $0.7 < MM(ep \to e'K^+K^-X) < 1.1$ GeV cut

Fig. 3.7 $MM(ep \to e'K^+K^-X)$ (a), $MM(ep \to e'pK^-X)$ (b) and $MM(ep \to e'pK^+X)$ (c) before (left) and after (right) a cut of $0.7 < MM(ep \to e'K^+K^-X) < 1.1$ GeV was imposed. A cut of $|MM^2(ep \to e'pK^+K^-X)| < 0.01$ GeV^2 has been imposed on all data shown.

3.2.3 Comparison with sPlots

Another method of background removal is known as the *sPlot* technique. This method required using a fitting function to fit a discriminating variable, y, in order to calculate weights known as *sWeights*. The fitting and calculation of *sWeights* was completed using a program known as brufit

[43]. The yields of the sources of events, N_s, are extracted by fitting the discriminating variable using a maximum likelihood fit which has an associated covariance matrix, V_{nj}.

The discriminating variable chosen was the missing proton mass. This variable was fitted using a fitting function based on simulated data, which will be elaborated on in Sec. 3.3, for the signal part and a third-order polynomial for the background part. 2000 bins were used to produce a smooth fit, which is shown in Fig. 3.8a. By making use of the covariance matrix associated with this fit, the *sWeights* were calculated using

$$P_n(y) = \frac{\sum_{j=1}^{N_s} V_{nj} f_j(y)}{\sum_{k=1}^{N_s} N_k f_k(y)}, \tag{3.12}$$

where N is the yield of the event source and f is the fitting function for the j and k components of the data. The *sWeights* were then used to reweight the event, based on whether it was more likely a signal or background event. The weights were applied to the missing K^+ and K^- masses, which are shown in Fig. 3.8b. It can be seen that the background is removed using the *sPlot* technique just as it is removed for the missing mass cut technique shown in Fig. 3.7.

The *sPlot* technique can be used as the primary method of background removal; however, this technique introduces errors during the moment extraction process. Further work is required to reduce these errors which could be a focus of future research.

3.3 Simulations

Simulations were used to obtain information on the detector that could not be extracted from experimental data, such as the CLAS12 detector acceptance. Simulated events for the $ep \rightarrow epK^+K^-$ reaction were generated using the CLAS12-elSpectro program [44]. This program generated events using Monte-Carlo (MC) simulations which were then passed through a realistic simulation of the CLAS12 detector using the Geant4 Monte Carlo (GEMC) program which is a part of CLAS12-elSpectro.

3.3.1 Acceptance

The phase space of a reaction contains all possible physical spaces where particles can be found based on energy and momentum conservation laws. Due to the design of CLAS12, the angular range is limited meaning only events in a certain range of the phase space can be detected. The acceptance is the ratio of the number of events in the reaction that can be detected by CLAS12 to the total number

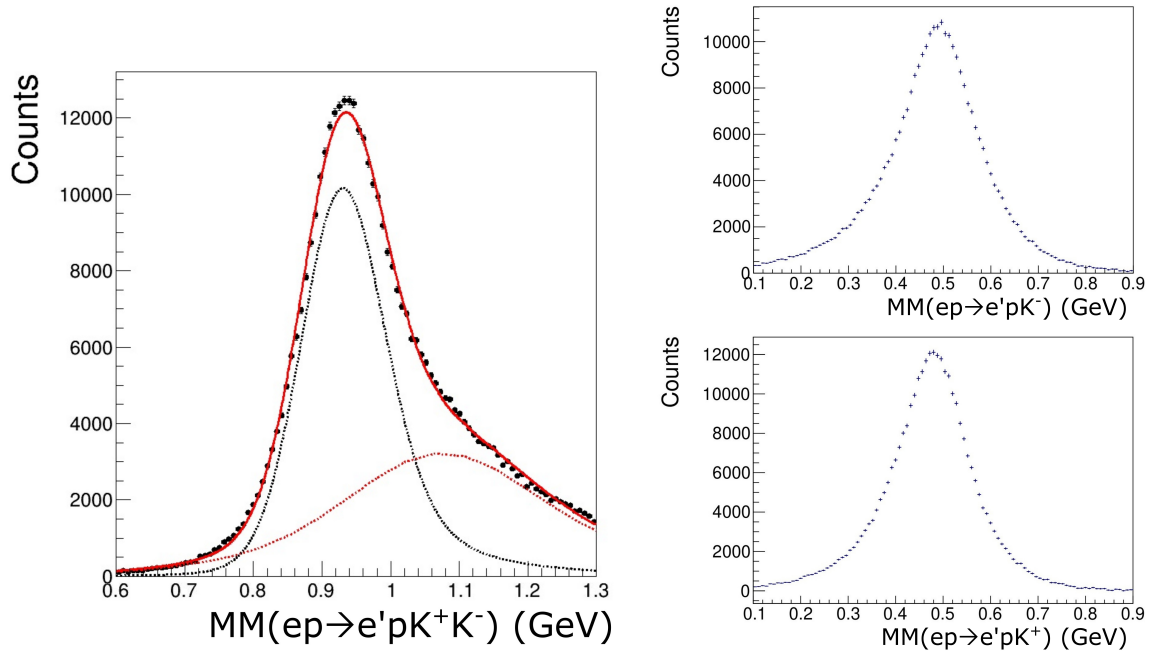

(a) An *sPlot* fit of $MM(ep \to e'K^+K^-X)$

(b) $MM(ep \to e'pK^-X)$ (top) and $MM(ep \to e'pK^+X)$ (bottom) masses reweighted using sWeights.

Fig. 3.8 *sPlot* fit of $MM(ep \to e'pK^+K^-X)$ (a), the solid red line is the fit of the data which is made up of the black dashed line corresponds to the function that was used to fit the signal peak and the red dashed line corresponds to the third-order polynomial that was used to fit the background. Missing mass plots (b) for $MM(ep \to e'pK^-X)$ (b, top) and $MM(ep \to e'pK^+X)$ (b, bottom) masses reweighted using sWeights.

of events. The acceptance can be defined for any kinematic variable such as missing mass or polar angle. CLAS12-elSpectro was used to calculate acceptance by comparing the pure MC simulated data and the GEMC simulated data. Knowing the acceptance of the detector allowed for the effect of the detector's physical features on the data to be studied and accounted for. In Section 4.1.2, the simulated data are used extensively in understanding the experimental data.

3.3.2 Comparison with Data

The simulated data must match closely to the experimental data so that properties of the detector, such as acceptance and efficiency, are calculated correctly and for the reaction of interest. To ensure the simulated and experimental were alike, several properties of these data were compared. The first property that was compared was the Mandelstam variable t, which relates the energy and momentum transferred from the beam to the target during an interaction. t can be calculated by considering the

transfer of energy and momentum from the target to the scattered proton or from the beam to the scattered electron and meson. In the latter, the decay products of the meson are detected so it is information on these decay products that are used to calculate t. The first calculation of t is given by

$$t_1 = \sqrt{(|P_t - P_p|^2)} = \sqrt{(m_t - E_p)^2 - |\bar{p}_p|^2}, \tag{3.13}$$

and the second is given by

$$\begin{aligned} t_2 &= \sqrt{|P_b - (P_{e'} + P_{K^+} + P_{K^-})|^2} \\ &= \sqrt{(E_b - (E_{e'} + E_{K^+} + E_{K^-}))^2 + |\bar{p}_e - (\bar{p}_{e'} + \bar{p}_{K^+} + \bar{p}_{K^-})|^2}. \end{aligned} \tag{3.14}$$

If an event has been identified and reconstructed correctly then t_1 should be equal to t_2. This is shown in Fig. 3.9, where it can be seen that t_1 and t_2 become more comparable after imposing event selection cuts and after reaction reconstruction for the experimental data. The difference between t_1 and t_2 is due to the momentum and energy resolution of CLAS12 when detecting different types of particles which introduce uncertainties into the calculations of t_1 and t_2.

A similar comparison can be made between the simulated and experimental data. If the simulated and experimental data are similar then t_1 and t_2 should be similar. Another important comparison between the experimental and simulated data is the similarity of the electron momentum and photon polarisation. All of these comparisons are shown in Fig. 3.10. After imposing event selection cuts and after reaction reconstruction, it can be seen that the simulated and experimental data are comparable as required.

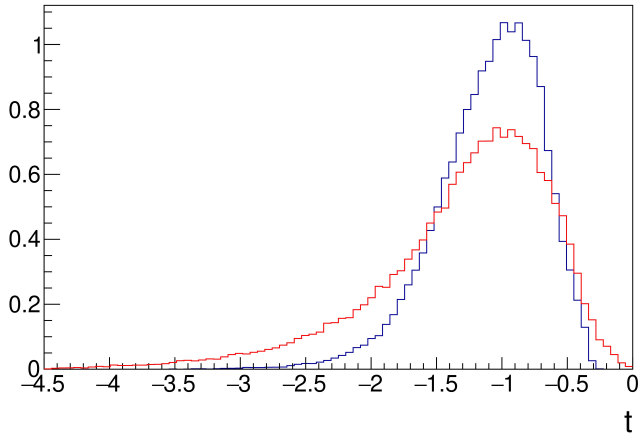

(a) t before cuts

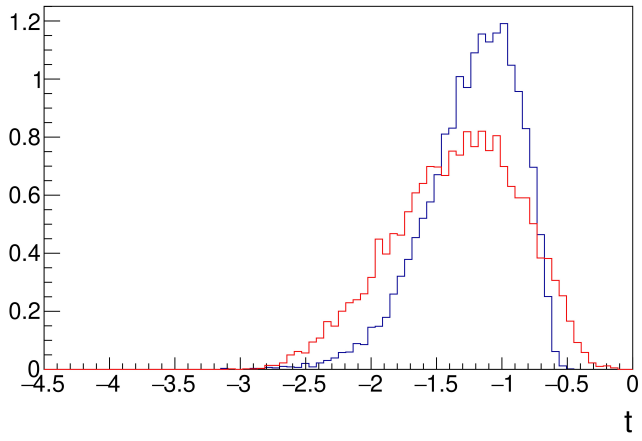

(b) t after event selection cuts

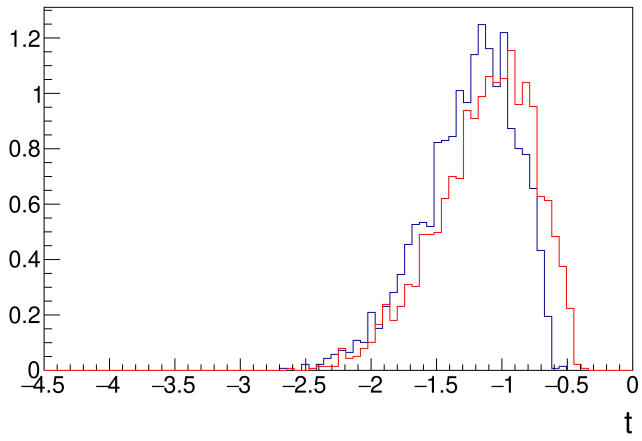

(c) t after reaction reconstruction

Fig. 3.9 t_1 (blue) and t_2 (red) from experimental data before cuts (a), after event selection cuts: $2.0^\circ < \theta < 5.0^\circ$ and $0.4 < E_e < 5.0$ GeV (b), and after event selection cuts and after reaction reconstruction: $0.7 < MM(ep \to e'K^+K^-X) < 1.1$ GeV and $|MM^2(ep \to e'pK^+K^-X)| < 0.01$ GeV^2 (c).

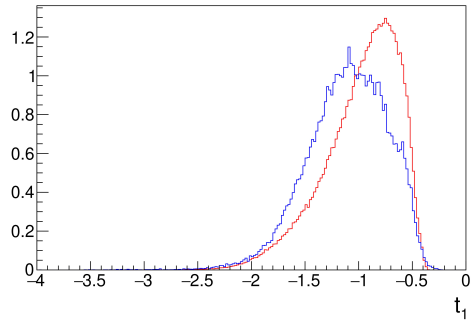

(a) t_1 before cuts

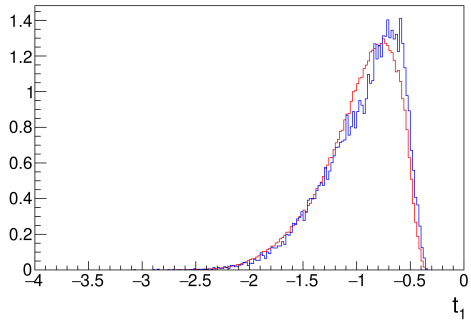

(b) t_1 after cuts

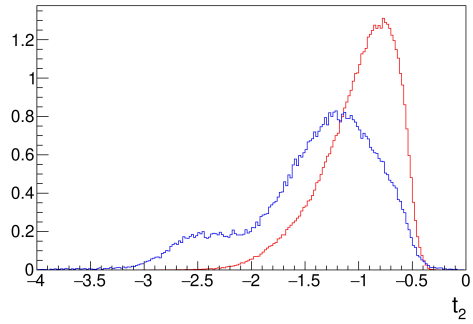

(c) t_2 before cuts

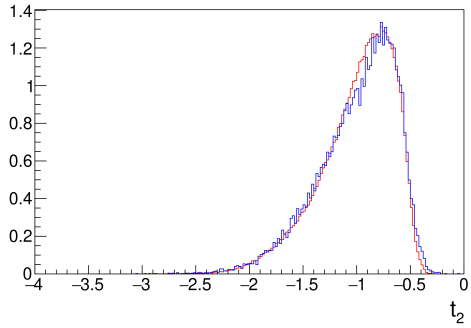

(d) t_2 after cuts

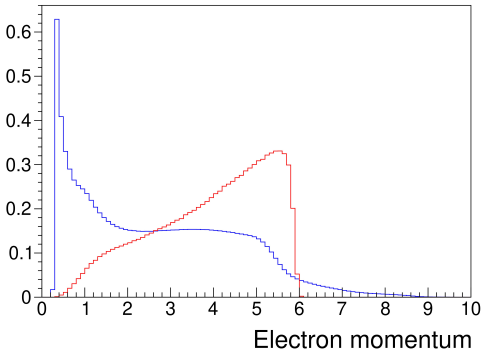

(e) Electron momentum before cuts

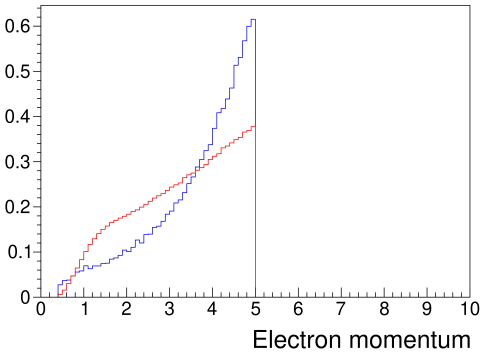

(f) Electron momentum after cuts

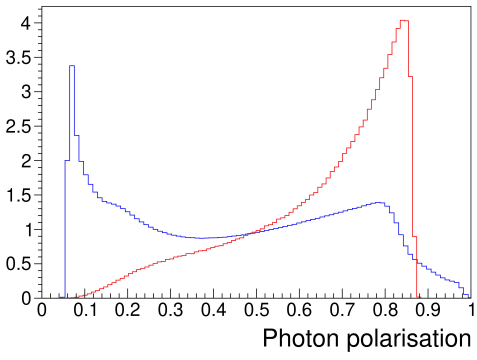

(g) Photon polarisation before cuts

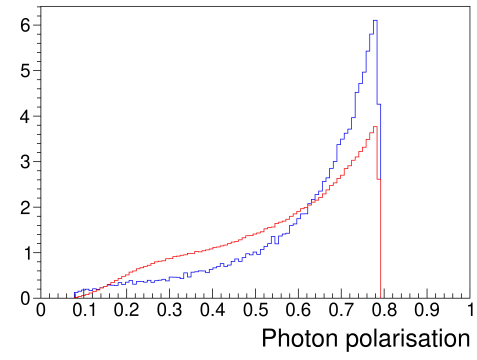

(h) Photon polarisation after cuts

Fig. 3.10 t_1 (a,b), t_2 (c,d), electron momentum (e,f) and photon polarisation (g,h) before and after event selection cuts and reaction reconstruction from experimental (blue) and simulated (red) data.

Chapter 4

Results

This chapter details the process of extracting moments from the data and the final results are presented. Information on the angle between the K^+ and K^- was obtained and used to extract the moments across a range of K^+K^- invariant mass bins using the brufit program [43].

4.1 Angular Distributions and Polarisation

Angular distributions show the scattering behaviour of the K^+ and K^- which gives insight into the parent meson. Distributions were obtained for the angles θ_{K^+}, ϕ_{K^+} and Φ which belong to a frame of reference known as the Gottfried-Jackson frame. This frame is generally used for photoproduction reactions in which a resonance is produced and then decays into two mesons. The polarisation of the photon is vital in calculating Φ. Since the photon is not detected, its polarisation was calculated using Eq. (3.8), which requires information on the scattered electron.

4.1.1 Gottfried-Jackson Frame

A frame of reference is any coordinate system used to describe and study the motion of objects in a system. The laboratory or lab frame, Fig. 4.1a, is defined to have the incoming photon travelling along the z_{Lab} axis in the $+z$ direction and impinging off a stationary target, producing a meson which travels in the $+z$ direction. In this frame, the y_{Lab} axis is defined in the up direction and the x_{Lab} axis is perpendicular to the plane formed by z_{Lab} and y_{Lab} axes.

Another frame, known as the centre-of-mass (CM) frame, Fig. 4.1b, has the same axes as the lab frame but a Lorentz boost is applied so that the whole frame moves in the $+z$ direction compared to the

lab frame. A Lorentz boost is used as the system is moving at relativistic speeds. In the centre-of-mass frame, the products travel in opposite directions and at speeds such that the total momentum of the system is zero.

The frame used in the research presented in this is known as the Gottfried-Jackson (GJ) frame, Fig. 4.1c. A Lorentz boost from the centre of mass frame to the rest frame of the meson is performed, and the decay products of the meson are included. In this frame, the direction of the photon defines the z_{GJ} axis. The photon and the scattered proton form the reaction plane which the x_{GJ} axis lies along and to which the y_{GJ} axis is perpendicular. The x_{GJ}, y_{GJ} and z_{GJ} axes are given by,

$$x_{GJ} = y_{GJ} \times z_{GJ}, \qquad y_{GJ} = \frac{p_\gamma \times p_{p'}}{|p_\gamma \times p_{p'}|}, \qquad z_{GJ} = \frac{p_\gamma}{|p_\gamma|}, \tag{4.1}$$

where p_γ and $p_{p'}$ are vectors of photon and scattered proton, respectively [45]. In the GJ frame, the meson decays seemingly at rest, allowing for angles of the decay products to be easily defined. Two important GJ angles are the polar angles of K^+, $(\theta_{K^+}, \phi_{K^+})$, which are given by

$$\theta_{K^+} = \cos^{-1}\left(\frac{p_{K^+} \cdot z_{GJ}}{|p_{K^+}|}\right), \qquad \phi_{K^+} = \cos^{-1}\left(\frac{y_{GJ} \cdot (p_{K^+} \times z_{GJ})}{|p_{K^+} \times z_{GJ}|}\right), \tag{4.2}$$

where p_{K^+} is the vector of the K^+. These two angles are referred to by the solid angle $\Omega_{K^+} = (\theta_{K^+}, \phi_{K^+})$. Another important angle is the angle formed by the photon polarisation vector P and the reaction plane [46]. All three of these angles are shown in Fig. 4.1d.

4.1.2 Fitting Distributions

Distributions of the angles θ_{K^+}, ϕ_{K^+} and Φ and the polarisation of the photon, P, were obtained for the experimental and simulated data. Moments extraction required the simulated data to be correctly fitted to the experimental data for each of the variables. This was accomplished using the MINUIT2 program which utilises log-likelihood methods to find the minimum of a function and then analyses the function about this minimum. This program is suited to work on multi-parameter functions where the parameters may be correlated, making it ideal for the analysis presented in this thesis [47]. The successful fitting of the simulated data to the experimental data is shown in Fig. 4.2, it can be seen that the experimental and simulated variables are comparable as required.

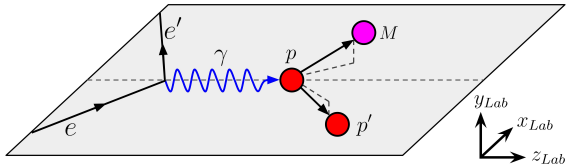

(a) The system in the lab frame

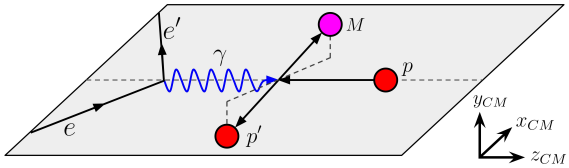

(b) The system in the CM frame

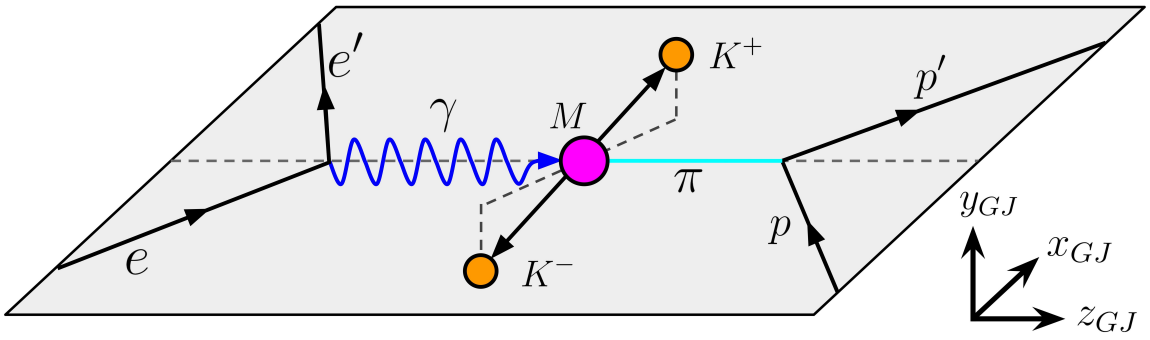

(c) The system in the GJ frame

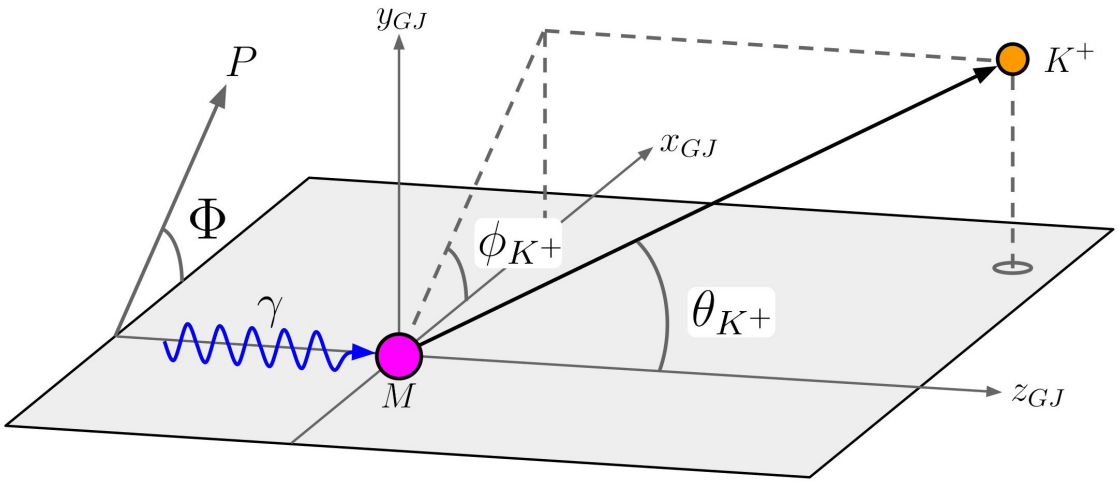

(d) Angles in the GJ frame

Fig. 4.1 The system in the lab (a) and CM (b) frames. The system in the GJ frame (c) showing the reaction plane (grey) and the meson (magenta) decaying at rest into K^+ and K^- (both orange). The system GJ frame showing only the photon (blue), meson and K^+ (d). The angles shown are: θ_{K^+}, the polar angle of K^+ which is the angle between K^+ and the z axis; ϕ_{K^+}, the azimuthal angle of K^+; and Φ, the angle formed between the photon polarisation vector P and the reaction plane (grey).

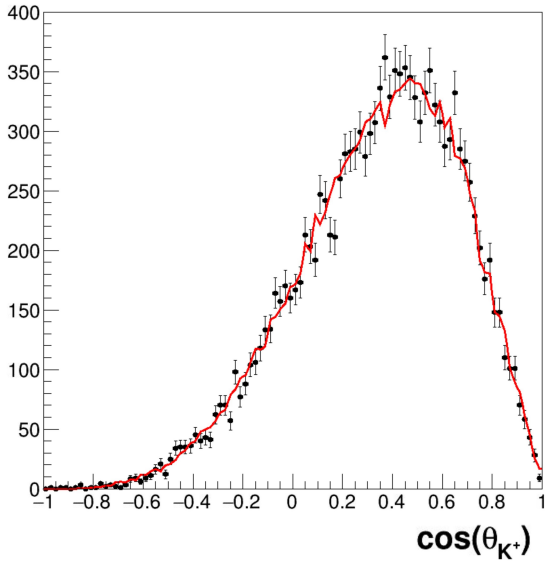

(a) A plot of the $\cos(\theta_{K^+})$ GJ angle

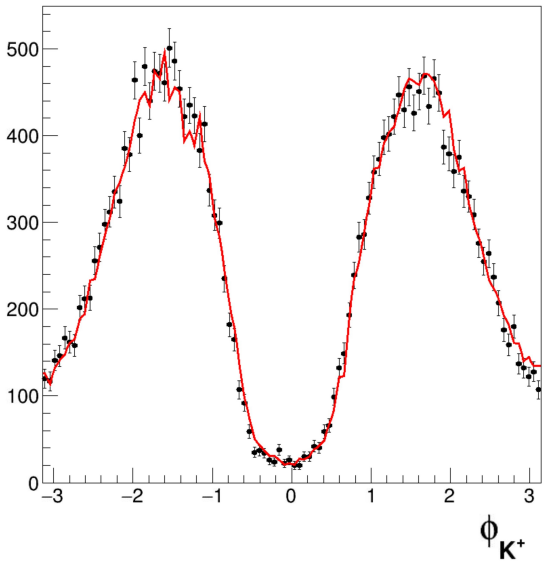

(b) A plot of the ϕ_{K^+} GJ angle

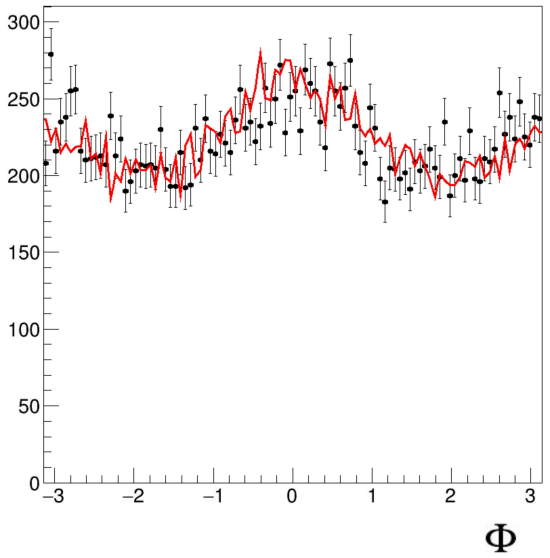

(c) A plot of the Φ GJ angle

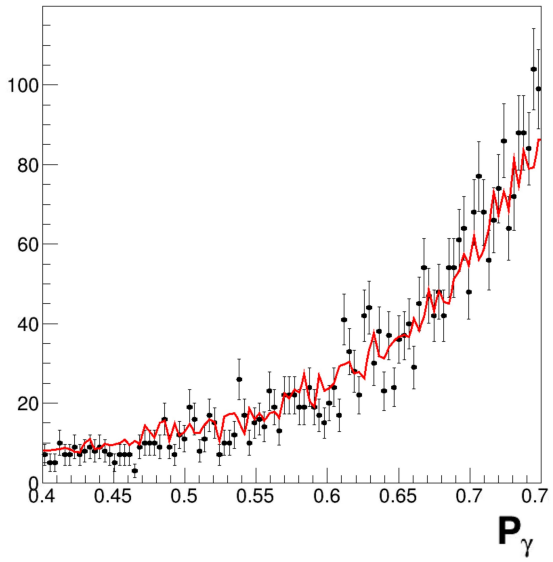

(d) A plot of the photon polarisation, P_γ

Fig. 4.2 Plots of $\cos(\theta_{K^+})$ (a), ϕ_{K^+} (b), Φ (c) and P_γ (d). The simulated data (red) is fitted to the experimental data (black). Plots were created using different K^+K^- invariant mass bins in order to demonstrate the correct fitting across the K^+K^- invariant mass range.

4.2 Moments Extraction

The data were split into K^+K^- invariant mass bins and then the moments were extracted for the data in each bin. Moments were extracted independently for each bin, reducing the effect of the overlapping of broad resonances.

4.2.1 Invariant Mass Binning

The K^+K^- invariant mass is the Lorentz-invariant total mass of K^+ and K^-, it is equivalent to the invariant mass of the meson, M_M, and is given by,

$$IM(K^+K^-) = M_M = |P_{K^+} + P_{K^-}| = \sqrt{(E_{K^+} + E_{K^-})^2 - |\bar{p}_{K^+} + \bar{p}_{K^-}|^2}. \tag{4.3}$$

K^+K^- invariant mass bins of equal width were used to split the experimental and the simulated data between 1.05 and 2.65 GeV. Splitting the data into bins allowed for resonances of different masses to be studied across the entire invariant mass range.

4.2.2 Unpolarised and Polarised Moments

The moments of the meson angular distribution are a set of functions that contain the contributions of the S, P and D partial waves belonging to the mesons that were produced in the reaction. Moments can be derived using the intensity and the GJ angles as shown in [48], a summary of this derivation follows.

The intensity of the reaction $ep \to e'pK^+K^-$ depends on the GJ angles; therefore, it is denoted $I(\Omega_{K^+},\Phi)$ and given by

$$I(\Omega_{K^+},\Phi) = \frac{d\sigma}{dtdmd\Phi} = \kappa \sum_{\lambda,\lambda',\lambda_{K^+},\lambda_{K^-}} A_{\lambda;\lambda_{K^+},\lambda_{K^-}}(\Omega_{K^+}) \rho^{\gamma}_{\lambda,\lambda'}(\Phi) A^*_{\lambda;\lambda_{K^+},\lambda_{K^-}}(\Omega_{K^+}), \tag{4.4}$$

where the middle term in the differential cross-section, κ is the phase space factor, $A_{\lambda;\lambda_{K^+},\lambda_{K^-}}$ is the amplitude of the reaction, λ is the helicity of the denoted particle, and $\rho^{\gamma}_{\lambda,\lambda'}$ is the density matrix of the photon. Two types of moments can be defined: polarised, $H^0(LM)$, and unpolarised, $H^1(LM)$ and $H^2(LM)$. The density matrix may be explicitly or implicitly dependent on the polarisation angle Φ,

for $H^0(LM)$ it is implicit and for $H^1(LM)$ and $H^2(LM)$ it is explicit. The moments are given by

$$H^0(LM) = \frac{1}{2\pi}\int_0^{2\pi}\int_0^{2\pi}\int_{-1}^{1}(\Omega_{K^+},\Phi)d^L_{M0}(\theta_{K^+})\cos(M\phi_{K^+})d(\cos\theta_{K^+})d\phi_{K^+}d\Phi, \tag{4.5a}$$

$$H^1(LM) = \frac{1}{P_\gamma\pi}\int_0^{2\pi}\int_0^{2\pi}\int_{-1}^{1}(\Omega_{K^+},\Phi)d^L_{M0}(\theta_{K^+})\cos(M\phi_{K^+})\cos(2\Phi)d(\cos\theta_{K^+})d\phi_{K^+}d\Phi, \tag{4.5b}$$

$$\mathrm{Im}H^2(LM) = \frac{-1}{P_\gamma\pi}\int_0^{2\pi}\int_0^{2\pi}\int_{-1}^{1}(\Omega_{K^+},\Phi)d^L_{M0}(\theta_{K^+})\sin(M\phi_{K^+})\sin(2\Phi)d(\sin\theta_{K^+})d\phi_{K^+}d\Phi, \tag{4.5c}$$

where L is the meson's angular momentum, equivalent to L in Sec. 1.2, and M is the meson's spin projection. A pair of L and M defines a unique moment and due to parity conservation, $0 \leq M \leq L$. The moments can be written in terms of partial waves by using the wave set

$$\left\{S_0^{(+)}, P_{0,1}^{(+)}, D_{0,1,2}^{(+)}\right\}, \tag{4.6}$$

where S waves correspond to spin 0 mesons, P waves correspond to spin 1 mesons and D waves correspond to spin 2 mesons. In Eq. (4.6), the $+$ symbol refers to the reflectivity which is positive for all waves in Eq. (4.6). The moments contain the contributions of the S, P and D waves from the mesons produced in the reaction; however, further analysis is required to extract the quantum numbers, such as angular momentum, of the individual mesons produced in the reaction. Thus, moments extraction is an important technique for investigating exotic mesons.

For the wave set given by Eq. (4.6), moments can be extracted up to $L = M = 4$. Therefore, in the research presented in the thesis, moments for were extracted from $L = M = 0$ up to $L = M = 4$ for $H^0(LM)$, $H^1(LM)$ and $H^2(LM)$, using Eq. (4.5a), Eq. (4.5b) and Eq. (4.5c), respectively. For example, $H^0(00)$ is given by

$$H^0(00) = H^1(00) + 2\left[|P_1^{(+)}|^2 + |D_1^{(+)}|^2 + |D_2^{(+)}|^2\right], \tag{4.7}$$

and $H^1(00)$ is given by

$$H^1(00) = 2\left[|S_0^{(+)}|^2 + |P_0^{(+)}|^2 + |D_0^{(+)}|^2\right]. \tag{4.8}$$

The full sets of $H^0(LM)$ and $H^1(LM)$ up to $L = M = 4$ are given in Appendix A.

4.3 Results

The first sets of moments were extracted across 10 K^+K^- invariant mass bins. The unpolarised moments are shown in 4.3 and the polarised moments are shown in 4.4. Initially, 10 bins were chosen in order to observe general trends across the whole invariant mass range.

40 bins were used to extract moments across smaller mass ranges in order to more closely examine fluctuations and sign changes of the moments. However, a higher number of bins means there is less data per bin, resulting in poorer fitting for bins with low statistics. The results for the unpolarised and the polarised moments are shown in Fig. 4.5 and Fig. 4.6, respectively. In these distributions, it can be seen that uncertainties are greater for the higher mass bins due to the lower amount of data in these bins compared to the lower mass bins. The effect of changing the amount of data per bin on the uncertainty can also be seen by comparing Fig. 4.3 and Fig. 4.3. Each of the 10 bins in Fig. 4.3 has a greater amount of data than each bin in Fig. 4.3 and as a result, uncertainties are much lower. A very high number of bins would reduce the data in the lower mass bins, increasing the uncertainty in these bins; therefore, 40 bins was the maximum number of bins used.

The equations for $H^0(10)$ and $H^1(00)$, Eq. (A.1b) and Eq. (A.1a), respectively, consist of the squared magnitudes of the partial waves. Therefore, these moments should be greater than zero which

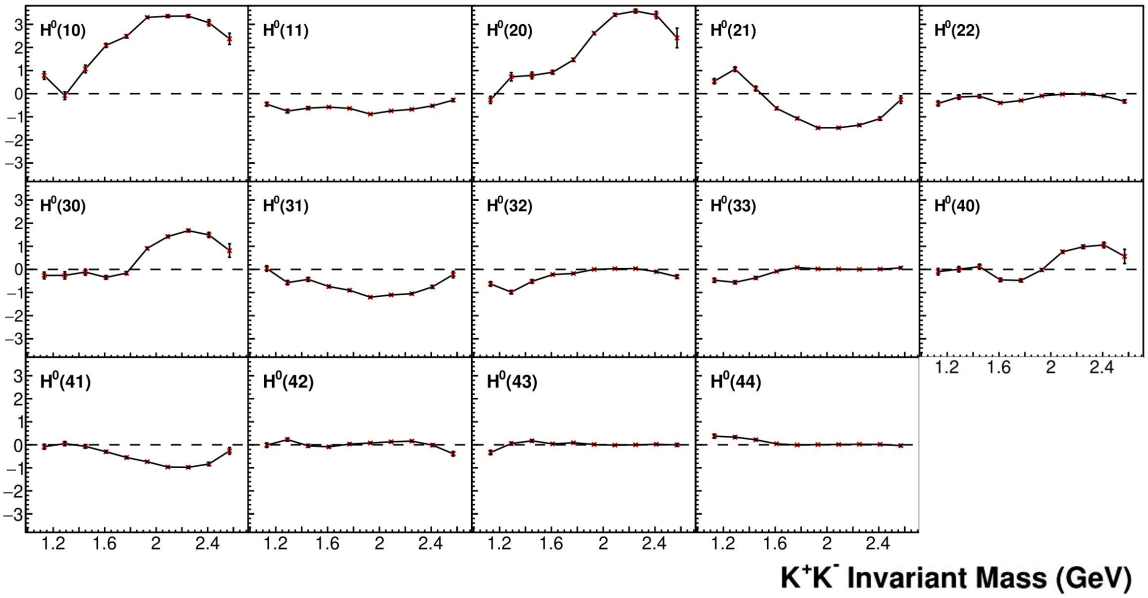

Fig. 4.3 H^0 moments across 10 bins of K^+K^- invariant mass

is seen in Fig. 4.5 and Fig. 4.6, within the provided error bars, meaning that the moments have been extracted correctly.

Although these results are preliminary, some conclusions can be drawn from the extracted moments. The equation for $H^1(30)$, Eq. (A.1g), consists of only P and D waves. Therefore, there may be some contributions from the $f_2(1270)$ and $f_2'(1525)$ mesons, which are both spin 2. The $f_2(1270)$ has a mass of 1.275 GeV and $f_2'(1525)$ has a mass of 1.517 GeV; both decay into K^+K^- with branching ratios of 4.6% and 88%, respectively [3]. In Fig. 4.7, the $H^1(30)$ moment is shown with vertical lines drawn at the masses of the $f_2(1270)$ and $f_2'(1525)$. At both masses, there are peaks indicating possible contributions from the $f_2(1270)$ and $f_2'(1525)$ mesons. The process of extracting quantum numbers of moments requires extensive theoretical work and data from other scattering experiments. This work is done by theorists at the Joint Physics Analysis Center (JPAC). Furthermore, a detailed systematic study needs to be conducted on the effect of each cut to evaluate the sensitivity of the moments.

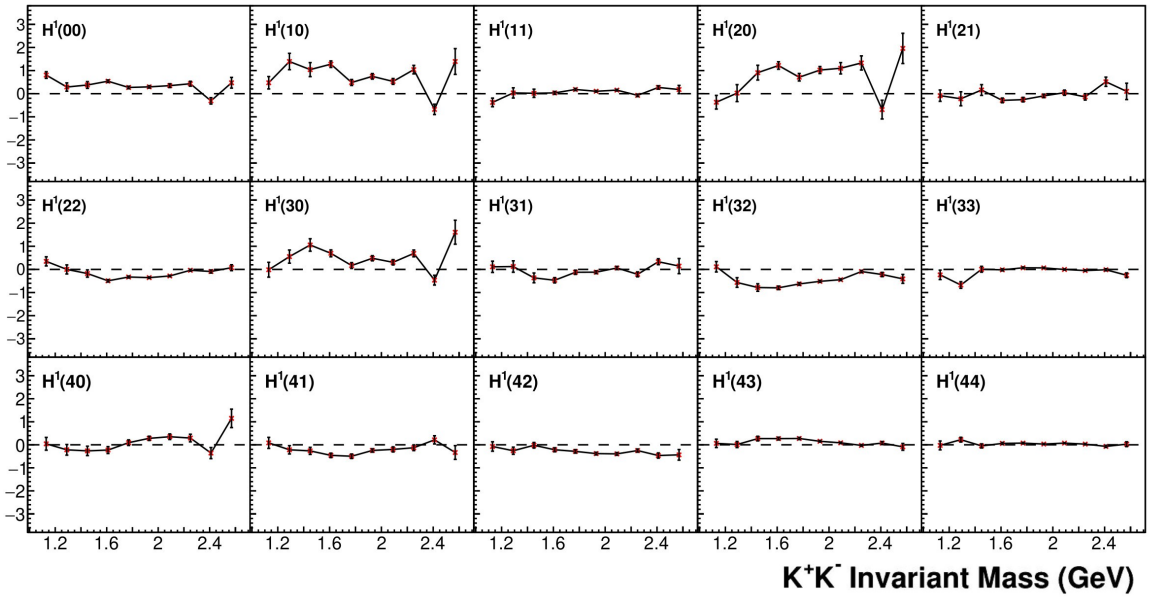

(a) H^1 moments - 10 bins

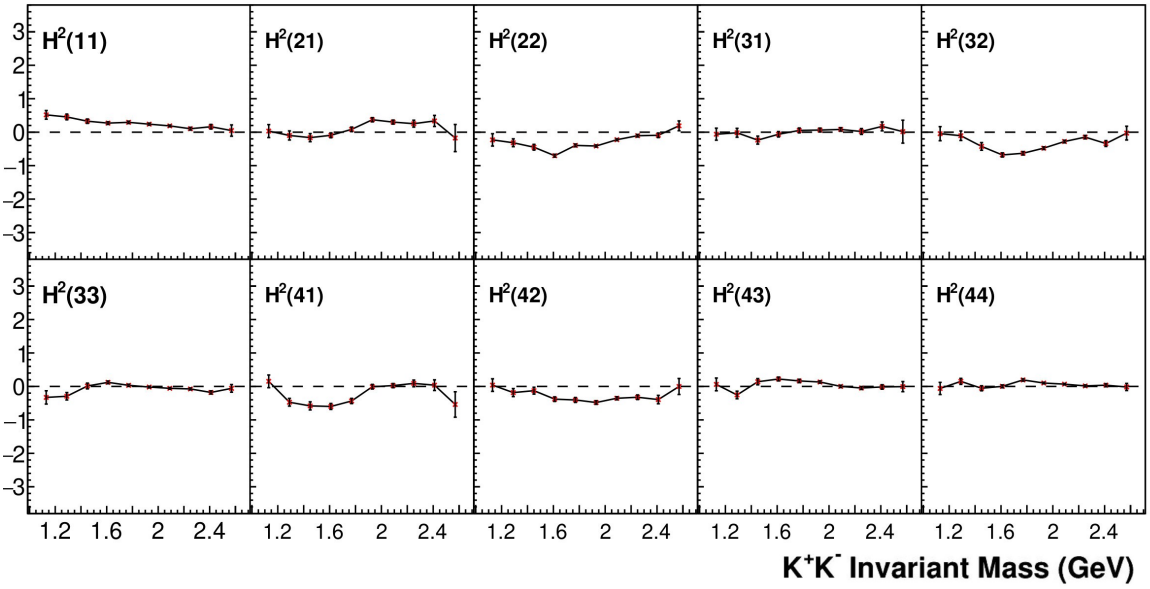

(b) H^2 moments - 10 bins

Fig. 4.4 H^1 and H^2 moments across 10 bins of K^+K^- invariant mass

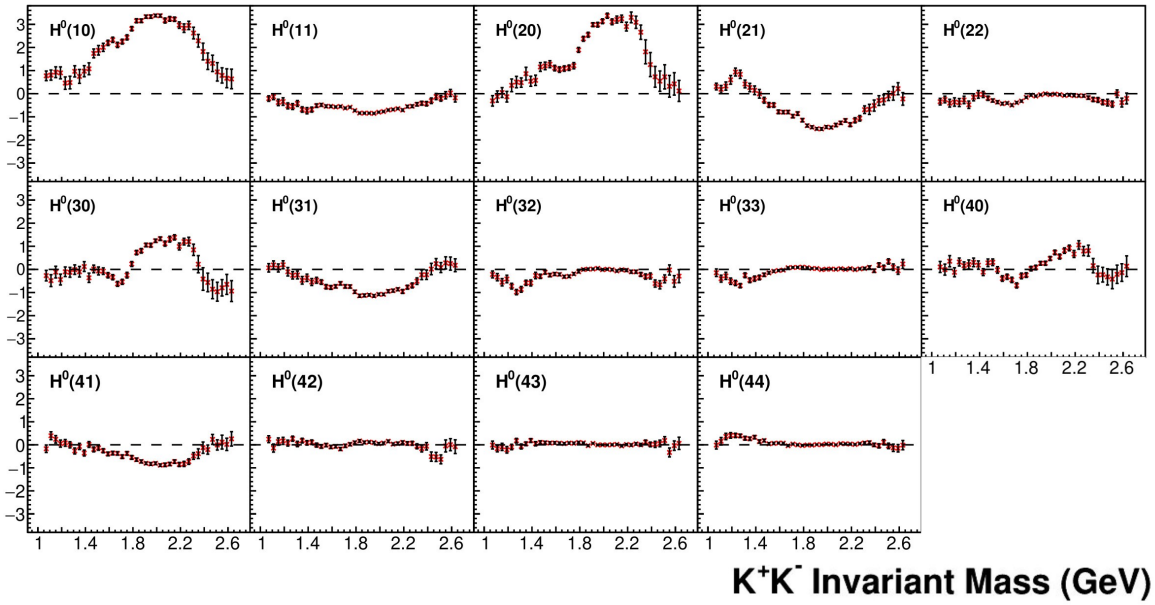

Fig. 4.5 H^0 moments across 40 bins of K^+K^- invariant mass

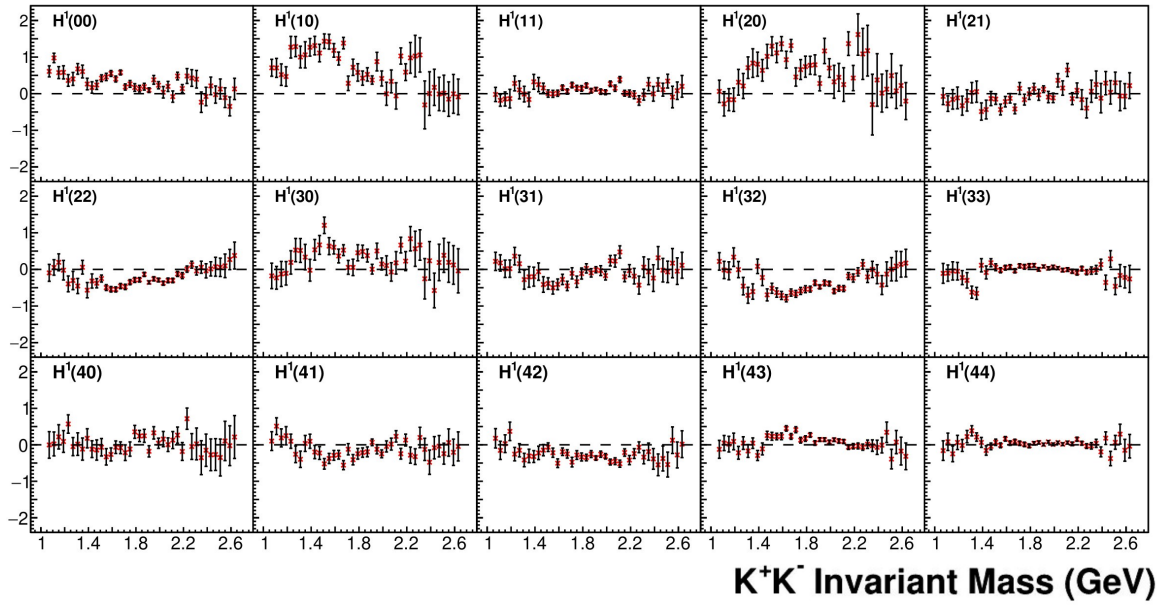

(a) H^1 moments - 40 bins

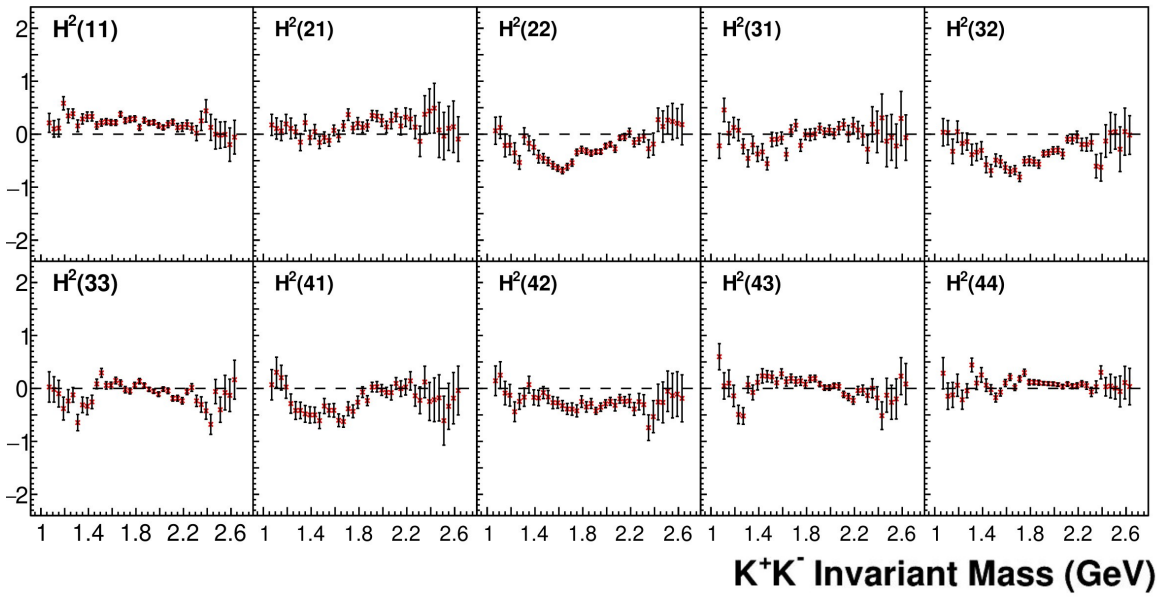

(b) H^2 moments - 40 bins

Fig. 4.6 H^1 and H^2 moments across 40 bins of K^+K^- invariant mass

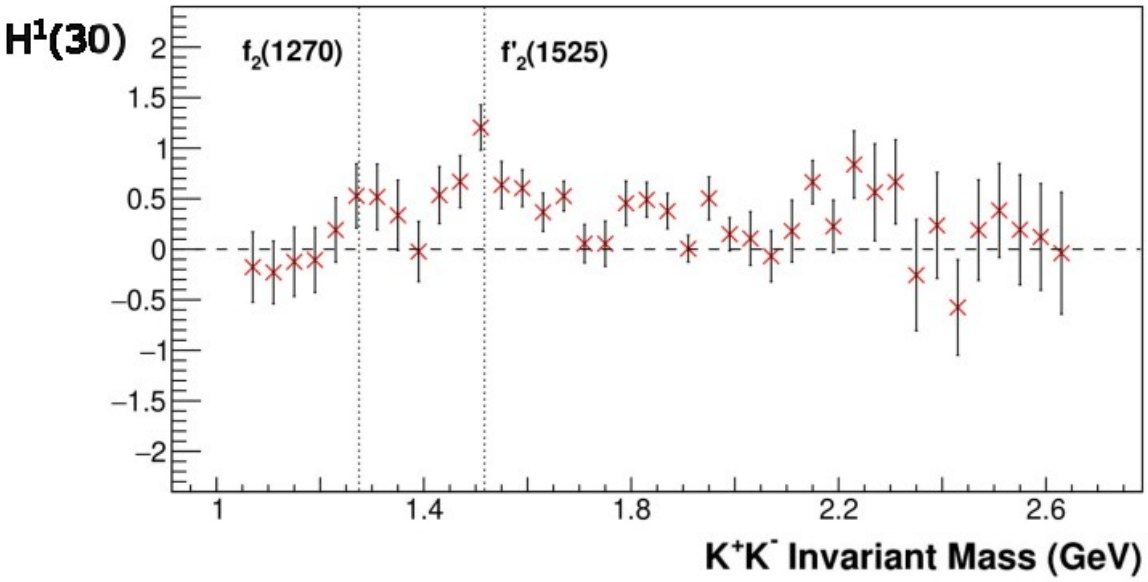

Fig. 4.7 $H^1(30)$ moment across 40 bins of K^+K^- invariant mass. Vertical lines are drawn at the masses of the $f_2(1270)$ and $f_2'(1525)$, the peaks at these masses indicate possible contributions from the $f_2(1270)$ and $f_2'(1525)$ spin 2 mesons.

Chapter 5

Conclusion

In the research presented in this thesis, moments of angular distribution were extracted for the epK^+K^- final state from data produced at Jefferson Lab using CLAS12. A 10.2 GeV electron beam was struck against a liquid hydrogen target to produce a variety of particles which were detected by CLAS12. The Forward Tagger was used to measure electrons scattered at low angles which correspond to quasi-real photoproduction reactions. The moments provide the contributions of spin 0, 1 and 2 mesons to the final state and were formulated for the epK^+K^- final state in terms of the S, P and D partial waves.

Data from Run Group A collected in Spring 2019 were used in the research presented in this thesis. The analysis of data involved event selection and reaction reconstruction. Event selection was conducted in order to remove misidentified particles and reduce the number of particles; techniques included topology selections, a χ^2_{PID} cut and a Δt cut. Then reaction reconstruction was conducted in order to remove events that did not correspond to the reaction of interest. Once the data were filtered so that only events corresponding to the epK^+K^- final state were retained, distributions of the Gottfried-Jackson angles were obtained. Simulated data were produced and compared to the experimental data to ensure both sets of data were similar. Then the simulated data were fitted to the experimental data and the moments were extracted. Moments were extracted for 10 bins and 40 bins of K^+K^- invariant mass between 1.05 and 2.65 GeV. The second unpolarised and first polarised moments, $H_0(10)$ and $H_1(00)$ respectively, display the expected behaviour; therefore, it was hypothesised as to which mesons contributed to the final state.

To say with certainty which mesons were present in the final state, the partial waves of these mesons are required. The partial waves can be extracted using the equation derived in [48], however,

this process is more complicated and requires further studies. The extraction of partial waves could be the focus of future research. Furthermore, the research presented in this thesis can be extended to other reactions, such as $ep \rightarrow epK^+K^-\pi^0$, in which exotic mesons may contribute to the final state. This research requires different a reaction reconstruction process and for new moments to be formulated for the $epK^+K^-\pi^0$ final state.

Bibliography

[1] B. Martin and G. Shaw, *Particle physics* (Wiley, United Kingdom, 2008).

[2] S. Chatrchyan et al., "Observation of a new boson at a mass of 125 gev with the cms experiment at the lhc", Physics Letters B **716**, 30–61 (2012), https://www.sciencedirect.com/science/article/pii/S0370269312008581.

[3] P. D. Group et al., "Review of Particle Physics", Progress of Theoretical and Experimental Physics **2022**, 083C01 (2022), https://doi.org/10.1093/ptep/ptac097.

[4] Y. Nambu, *Quarks: frontiers in elementary particle physics* (World Scientific, United Kingdom, 1985).

[5] M. Gell-Mann, "The eightfold way: a theory of strong interaction symmetry", in (1961), https://api.semanticscholar.org/CorpusID:118429725.

[6] M. Gell-Mann, "A schematic model of baryons and mesons", Physics Letters **8**, 214–215 (1964), https://www.sciencedirect.com/science/article/pii/S0031916364920013.

[7] H.-J. Behrend et al., "A measurement of the muon pair production in e+e annihilation at 38.3s46.8gev", Physics Letters B **191**, 209–216 (1987), https://www.sciencedirect.com/science/article/pii/0370269387913499.

[8] W. Chinowsky and J. Steinberger, "Absorption of negative pions in deuterium: parity of the pion", Phys. Rev. **95**, 1561–1564 (1954), https://link.aps.org/doi/10.1103/PhysRev.95.1561.

[9] D. J. Gross and F. Wilczek, "Ultraviolet behavior of non-abelian gauge theories", Phys. Rev. Lett. **30**, 1343–1346 (1973), https://link.aps.org/doi/10.1103/PhysRevLett.30.1343.

[10] H. D. Politzer, "Reliable perturbative results for strong interactions?", Phys. Rev. Lett. **30**, 1346–1349 (1973), https://link.aps.org/doi/10.1103/PhysRevLett.30.1346.

[11] D. Gross, E. Klempt, and J. Stanley, "50 years of quantum chromodynamics - introduction and review", Eur. Phys. J. C **83**, 1125 (2023), https://doi.org/10.1140/epjc/s10052-023-11949-2.

[12] K. Gottfried and F. Weisskopf, *Concepts of particle physics volume 2* (Oxford University Press, United Kingdom, 1986).

[13] A. Chodos et al., "New extended model of hadrons", Phys. Rev. D **9**, 3471–3495 (1974), https://link.aps.org/doi/10.1103/PhysRevD.9.3471.

[14] C. E. Carlson, T. H. Hansson, and C. Peterson, "Meson, baryon, and glueball masses in the mit bag model", Phys. Rev. D **27**, 1556–1564 (1983), https://link.aps.org/doi/10.1103/PhysRevD.27.1556.

[15] J. J. Dudek et al. (for Hadron Spectrum Collaboration), "Toward the excited isoscalar meson spectrum from lattice qcd", Phys. Rev. D **88**, 094505 (2013), https://link.aps.org/doi/10.1103/PhysRevD.88.094505.

[16] Y. Chen et al., "Glueball spectrum and matrix elements on anisotropic lattices", Phys. Rev. D **73**, 014516 (2006), https://link.aps.org/doi/10.1103/PhysRevD.73.014516.

[17] C. Bernard et al., "Exotic mesons in quenched lattice qcd", Phys. Rev. D **56**, 7039–7051 (1997), https://link.aps.org/doi/10.1103/PhysRevD.56.7039.

[18] T. Gutsche, "Exotic mesons in nucleon-antinucleon annihilation", Progress in Particle and Nuclear Physics **36**, Quarks In Hadrons And Nuclei, 427–435 (1996), https://www.sciencedirect.com/science/article/pii/0146641096000506.

[19] T. Gutsche, "Exotic mesons", Progress in Particle and Nuclear Physics **67**, From Quarks and Gluons to Hadrons and Nuclei, 380–389 (2012), https://www.sciencedirect.com/science/article/pii/S0146641011001657.

[20] C. Adolph et al., "Longitudinal double spin asymmetries in single hadron quasi-real photoproduction at high pt", Physics Letters B **753**, 573–579 (2016), https://www.sciencedirect.com/science/article/pii/S0370269315009831.

[21] A. Szczepaniak and M. Swat, "Role of photoproduction in exotic meson searches", Physics Letters B **516**, 72–76 (2001), https://api.semanticscholar.org/CorpusID:119441462.

[22] R. J. Jaffe, "Multiquark hadrons. i. phenomenology of $Q^2\overline{Q}^2$ mesons", Phys. Rev. D **15**, 267–280 (1977), https://link.aps.org/doi/10.1103/PhysRevD.15.267.

[23] C. A. Meyer and Y. Van Haarlem, "Status of exotic-quantum-number mesons", Phys. Rev. C **82**, 025208 (2010), https://link.aps.org/doi/10.1103/PhysRevC.82.025208.

[24] "Evidence for a 1+ exotic meson", Physics Letters B **205**, 397–400 (1988), https://www.sciencedirect.com/science/article/pii/0370269388916863.

[25] A. Abele et al., "Exotic state in pd annihilation at rest into 0 pspectator", Physics Letters B **423**, 175–184 (1998), https://www.sciencedirect.com/science/article/pii/S0370269398001233.

[26] M. G. Alekseev et al. (COMPASS Collaboration), "Observation of a $J^{\mathrm{PC}} = 1^{-+}$ exotic resonance in diffractive dissociation of 190 GeV$/c$ π^- into $\pi^-\pi^-\pi^+$", Phys. Rev. Lett. **104**, 241803 (2010), https://link.aps.org/doi/10.1103/PhysRevLett.104.241803.

[27] M. Ablikim et al. (BESIII Collaboration), "Determination of spin-parity quantum numbers of $X(2370)$ as 0^{-+} from $J/\psi \to \gamma K_S^0 K_S^0 \eta'$", Phys. Rev. Lett. **132**, 181901 (2024), https://link.aps.org/doi/10.1103/PhysRevLett.132.181901.

[28] Thomas Jefferson National Accelerator Facility, Department of Energy, https://www.energy.gov/ea/thomas-jefferson-national-accelerator-facility.

[29] C. W. Leemann, D. R. Douglas, and G. A. Krafft, "The continuous electron beam accelerator facility: cebaf at the jefferson laboratory", Annual Review of Nuclear and Particle Science **51**, 413–450 (2001), https://www.annualreviews.org/content/journals/10.1146/annurev.nucl.51.101701.132327.

[30] J. Arrington et al., "Physics with cebaf at 12 gev and future opportunities", Progress in Particle and Nuclear Physics **127**, 103985 (2022), https://www.sciencedirect.com/science/article/pii/S014664102200045X.

[31] V. Burkert et al., "The clas12 spectrometer at jefferson laboratory", Nuclear Instruments and Methods in Physics Research Section A: Accelerators, Spectrometers, Detectors and Associated Equipment **959**, 163419 (2020), https://www.sciencedirect.com/science/article/pii/S0168900220300243.

[32] M. Mamun et al., "Improved Electrostatic Design of the Jefferson Lab 300 kV DC Photogun and the Minimization of Beam Deflection", in Proc. 5th int. particle accel. conf. (napac'22), International Particle Accelerator Conference 5 (Oct. 2022), pp. 655–658.

[33] C. K. Sinclair et al., "Development of a high average current polarized electron source with long cathode operational lifetime", Phys. Rev. ST Accel. Beams **10**, 023501 (2007), https://link.aps.org/doi/10.1103/PhysRevSTAB.10.023501.

[34] M. Poelker et al., "Generation of electron bunches at low repetition rates using a beat-frequency technique", Phys. Rev. ST Accel. Beams **10**, 053502 (2007), https://link.aps.org/doi/10.1103/PhysRevSTAB.10.053502.

[35] A. Acker et al., "The clas12 forward tagger", Nuclear Instruments and Methods in Physics Research Section A: Accelerators, Spectrometers, Detectors and Associated Equipment **959**, 163475 (2020), https://www.sciencedirect.com/science/article/pii/S0168900220300838.

[36] A. Acker et al., "The clas12 micromegas vertex tracker", Nuclear Instruments and Methods in Physics Research Section A: Accelerators, Spectrometers, Detectors and Associated Equipment **957**, 163423 (2020), https://www.sciencedirect.com/science/article/pii/S0168900220300280.

[37] M. Mestayer et al., "The clas12 drift chamber system", Nuclear Instruments and Methods in Physics Research Section A: Accelerators, Spectrometers, Detectors and Associated Equipment **959**, 163518 (2020), https://www.sciencedirect.com/science/article/pii/S016890022030111X.

[38] P. K. Ghoshal et al., "Magnetic field mapping of the clas12 torus—a comparative study between the engineering model and measurements at jlab", IEEE Transactions on Applied Superconductivity **29**, 1–10 (2019).

[39] D. Carman et al., "The clas12 forward time-of-flight system", Nuclear Instruments and Methods in Physics Research Section A: Accelerators, Spectrometers, Detectors and Associated Equipment **960**, 163629 (2020), https://www.sciencedirect.com/science/article/pii/S0168900220302102.

[40] G. Asryan et al., "The clas12 forward electromagnetic calorimeter", Nuclear Instruments and Methods in Physics Research Section A: Accelerators, Spectrometers, Detectors and Associated Equipment **959**, 163425 (2020), https://www.sciencedirect.com/science/article/pii/S0168900220300309.

[41] V. Ziegler et al., "The clas12 software framework and event reconstruction", Nuclear Instruments and Methods in Physics Research Section A: Accelerators, Spectrometers, Detectors and Associated Equipment **959**, 163472 (2020), https://www.sciencedirect.com/science/article/pii/S0168900220300784.

[42] D. Glazier., Last accessed: 16/07/24, https://github.com/dglazier/chanser.

[43] D. Glazier., Last accessed: 23/07/24, https://github.com/dglazier/brufit.

[44] D. Glazier., Last accessed: 23/07/24, https://github.com/dglazier/clas12-elspectro/.

[45] W. A. Smith et al. (Joint Physics Analysis Center), "Ambiguities in partial wave analysis of two spinless meson photoproduction", Phys. Rev. D **108**, 076001 (2023), https://link.aps.org/doi/10.1103/PhysRevD.108.076001.

[46] V. Mathieu, "Moments of angular distribution in two mesons photoproduction", AIP Conference Proceedings **2249**, 030020 (2020), https://doi.org/10.1063/5.0008590.

[47] F. James and M. Winkler, Last accessed: 27/07/24, https://root.cern.ch/root/htmldoc/guides/minuit2/Minuit2.html.

[48] V. Mathieu et al. (Joint Physics Analysis Center Collaboration), "Moments of angular distribution and beam asymmetries in $\eta\pi^0$ photoproduction at gluex", Phys. Rev. D **100**, 054017 (2019), https://link.aps.org/doi/10.1103/PhysRevD.100.054017.

Appendix A

Moments in Terms of S, P and D Waves

The $H^0(LM)$ moments Re up to $L = M = 4$ in terms of the partial waves in Eq. 4.6 are given by

$$H^0(00) = H^1(00) + 2\left[|P_1^{(+)}|^2 + |D_1^{(+)}|^2 + |D_2^{(+)}|^2\right], \tag{A.1a}$$

$$H^0(10) = H^1(10) + \frac{4}{\sqrt{5}}\mathrm{Re}(P_1^{(+)}D_1^{(+)*}), \tag{A.1b}$$

$$H^0(11) = H^1(11) + 2\sqrt{\frac{2}{5}}\mathrm{Re}(P_1^{(+)}D_2^{(+)*}), \tag{A.1c}$$

$$H^0(20) = H^1(20) - \frac{2}{5}|P_1^{(+)}|^2 + \frac{2}{7}|D_1^{(+)}|^2 - \frac{4}{7}|D_2^{(+)}|^2, \tag{A.1d}$$

$$H^0(21) = H^1(21) + \frac{2\sqrt{6}}{7}\mathrm{Re}(D_1^{(+)}D_2^{(+)*}), \tag{A.1e}$$

$$H^0(22) = \frac{2}{\sqrt{5}}\mathrm{Re}(S_0^{(+)}D_2^{(+)*}) - \frac{4}{7}\mathrm{Re}(D_0^{(+)}D_2^{(+)*}), \tag{A.1f}$$

$$H^0(30) = H^1(30) - \frac{12}{7\sqrt{5}}\mathrm{Re}(P_1^{(+)}D_1^{(+)*}), \tag{A.1g}$$

$$H^0(31) = H^1(31) - \frac{2}{7}\frac{\sqrt{3}}{\sqrt{5}}\mathrm{Re}(P_1^{(+)}D_2^{(+)*}), \tag{A.1h}$$

$$H^0(32) = H^1(32) - \frac{2\sqrt{6}}{7}\mathrm{Re}(P_1^{(+)}D_2^{(+)*}), \tag{A.1i}$$

$$H^0(33) = 0, \tag{A.1j}$$

$$H^0(40) = H^1(40) - \frac{2}{21}\left[2|D_1^{(+)}|^2 - |D_2^{(+)}|^2\right], \tag{A.1k}$$

$$H^0(41) = H^1(41) - \frac{2\sqrt{5}}{21}\mathrm{Re}(D_1^{(+)}D_2^{(+)*}), \tag{A.1l}$$

$$H^0(42) = -\frac{2}{7}\frac{\sqrt{5}}{\sqrt{3}}\mathrm{Re}(D_0^{(+)}D_2^{(+)*}), \tag{A.1m}$$

$$H^0(43) = H^0(44) = 0. \tag{A.1n}$$

The $H^1(LM)$ moments Re up to $L = M = 4$ in terms of the partial waves in Eq. 4.6 are given by

$$H^1(00) = 2\left[|S_0^{(+)}|^2 + |P_0^{(+)}|^2 + |D_0^{(+)}|^2\right], \tag{A.1a}$$

$$H^1(10) = \frac{8}{\sqrt{15}}\mathrm{Re}(P_0^{(+)}D_0^{(+)*}) + \frac{4}{\sqrt{3}}\mathrm{Re}(S_0^{(+)}P_0^{(+)*}), \tag{A.1b}$$

$$H^1(11) = \sqrt{\frac{2}{5}}\mathrm{Re}(P_0^{(+)}D_1^{(+)*}) - \sqrt{\frac{2}{15}}\mathrm{Re}(P_1^{(+)}D_0^{(+)*}), \tag{A.1c}$$

$$H^1(20) = \frac{4}{5}|P_0^{(+)}|^2 + \frac{4}{7}|D_0^{(+)}|^2 - \frac{4}{\sqrt{5}}\mathrm{Re}(S_0^{(+)}D_0^{(+)*}) \tag{A.1d}$$

$$H^1(21) = \frac{2}{\sqrt{5}}\mathrm{Re}(S_0^{(+)}D_1^{(+)*}) + \frac{2\sqrt{3}}{5}\mathrm{Re}(P_0^{(+)}P_1^{(+)*}) + \frac{2}{7}\mathrm{Re}(D_0^{(+)}D_1^{(+)*}), \tag{A.1e}$$

$$H^1(22) = H^0(22) + \frac{\sqrt{6}}{7}|D_1^{(+)}|^2 + \frac{\sqrt{6}}{5}|P_1^{(+)}|^2, \tag{A.1f}$$

$$H^1(30) = \frac{12}{7}\sqrt{\frac{3}{5}}\mathrm{Re}(P_0^{(+)}D_0^{(+)*}), \tag{A.1g}$$

$$H^1(31) = \frac{4}{7}\sqrt{\frac{6}{5}}\mathrm{Re}(P_0^{(+)}D_1^{(+)*}) + \frac{6}{7}\frac{\sqrt{2}}{5}\mathrm{Re}(P_1^{(+)}D_0^{(+)*}), \tag{A.1h}$$

$$H^1(32) = \frac{2\sqrt{3}}{7}\left[\mathrm{Re}(P_0^{(+)}D_2^{(+)*}) + \sqrt{2}\mathrm{Re}(P_1^{(+)}D_1^{(+)*})\right], \tag{A.1i}$$

$$H^1(33) = \frac{6}{7}\mathrm{Re}(P_1^{(+)}D_2^{(+)*}), \tag{A.1j}$$

$$H^1(40) = \frac{4}{7}|D_0^{(+)}|^2, \tag{A.1k}$$

$$H^1(41) = \frac{2}{7}\sqrt{\frac{10}{3}}\mathrm{Re}(D_0^{(+)}D_1^{(+)*}), \tag{A.1l}$$

$$H^1(42) = H^0(42) + \frac{2\sqrt{10}}{21}|D_1^{(+)}|^2, \tag{A.1m}$$

$$H^1(43) = \frac{2}{3}\sqrt{\frac{5}{7}}\mathrm{Re}(D_1^{(+)}D_2^{(+)*}), \tag{A.1n}$$

$$H^1(44) = \frac{1}{3}\sqrt{\frac{10}{7}}|D_1^{(+)}|^2. \tag{A.1o}$$